Title: m⁶A-dependent FMRP control of DGKκ translation underlies core Fragile X phenotypes

Authors: Oktay Cakil[1*], Boglarka Zambo[1,2], Tatiana, Maroilley[1], Nathalie Drouot[1], Anastasiya Petrova[1], Luc Negroni[1], Gergo Gogl[1,2], Amélie Piton[1,3] & Hervé Moine[1*]

Affilitations:

1. Institut de Génétique et de Biologie Moléculaire et Cellulaire (IGBMC), Centre National de la Recherche Scientifique (CNRS UMR7104), Institut National de la Santé et de la Recherche Médicale (INSERM U1258), Université de Strasbourg, Illkirch 67400, France
2. Institut de Biologie Valrose - iBV, Université Côte d'Azur, CNRS UMR7277, Inserm, Nice, France.
3. Unité de Génétique Moléculaire, IGMA, Hôpitaux Universitaire de Strasbourg, Strasbourg, France

*Address for correspondence and material request: moine@igbmc.fr, cakilo@igbmc.fr

Competing interests

HM is listed as inventor on a patent describing the use of DGKκ for FXS therapy. All other authors declare no competing interests.

Abstract

Fragile X syndrome (FXS), a leading inherited cause of intellectual developmental disorder and autism, results from loss of the RNA-binding protein FMRP. Loss of FMRP causes excessive neuronal protein synthesis contributing to widespread functional disturbances, yet the mechanisms linking FMRP to specific mRNA targets remain unclear.

We show that FMRP promotes translation of the brain mRNA DGKκ by binding m⁶A-modified repetitive RNA motifs, thereby relieving a translational block encoded within its sequence. FMRP loss sharply reduces neuronal DGKκ, and DGKκ depletion alone reproduces hallmark FXS phenotypes, including hyperactivity, compulsive behavior, overgrowth, dendritic spine abnormalities, overactivated diacylglycerol signaling and increased protein synthesis. These findings identify DGKκ as a key effector of FMRP function and establish a regulatory axis where m⁶A RNA modification modulates neuronal translation. This work defines new principles of translational control in neurodevelopmental disorders and positions DGKκ as a central driver of FXS pathogenesis.

Introduction

Fragile X syndrome (FXS) is one of the most frequent monogenic causes of intellectual disability (ID) and autism spectrum disorders (ASD). FXS has a prevalence of about 1:5000 males and 1:8000 females and is associated with comorbidities including hyperactivity, anxiety, hypersensitivity, stereotypies, epilepsy, connective tissue dysplasia, macro-orchidism, post-natal overgrowth and post-puberty facial dysmorphism [1]. FXS is caused by the loss of expression or function of the *FMR1* gene encoding FMRP, an RNA binding protein implicated in very diverse biological functions such as chromatin remodeling, ion channel modulation, RNA stability, ribosome heterogeneity and translation regulation [2–10].

The *Fmr1*-KO mouse [11] recapitulates many FXS-like phenotypes (hyperactivity, altered anxiety, hypersensitivity, stereotypies, epilepsy, macro-orchidism, overgrowth, craniofacial anomalies) [12] associated to abnormal dendritic spine morphology across brain regions [13–17].

Global neuronal protein synthesis measurements show a net elevation in *Fmr1*-KO neurons [18–21], suggesting that FMRP primarily acts as a translational repressor. Although translational activation has paradoxically been reported for certain FMRP targets [22,23], the phenotypic alterations of the *Fmr1*-KO model are largely attributed to elevated neuronal protein synthesis due to loss of FMRP's translational control [12].

How FMRP selects its target mRNAs to achieve such widespread neuronal translation dysregulation effect remains incompletely understood. While studies suggested that FMRP associates with mRNAs on a transcriptome-wide scale via short sequence abundant motifs [24,25], other studies have identified specific mRNAs bound via more complex less frequent motifs [22,26,27], leaving FMRP's mRNA selection principles and translatome-wide impact unclear.

The diacylglycerol kinase kappa (*Dgkκ*) mRNA was evidenced as an mRNA most co-immunoprecipitated with FMRP in a CLIP (cross-linking and immunoprecipitation) assay

69 performed in primary murine cortical neurons [23,28]. Together with the fact that purified FMRP
70 binds *Dgkκ* mRNA with unprecedent affinity compared to other proposed targets, this
71 suggested that DGKκ might be a prominent target of FMRP and thus an important player in
72 FXS [23]. DGKκ protein level was found severely reduced in *Fmr1*-KO mouse and FXS brain
73 extracts while its RNA level was unaffected [23,28], indicating that FMRP is required for the
74 translation of DGKκ, in apparent contradiction with its primarily described function as a
75 translation repressor [29]. DGKκ could play an important role in FXS as it is a modulator of
76 diacylglycerol (DAG) and phosphatidic acid (PA), two second messenger lipids playing pivotal
77 roles in protein synthesis control and spine morphology dynamics and involved several
78 signaling pathways altered in FXS [30,31]. In agreement with a role in neuronal DAG signaling,
79 FMRP loss disrupts mGluRI-dependent DAG signaling-[23]. Moreover, treatment of young adult
80 *Fmr1*-KO mice with adeno-associated viral (AAV) vectors expressing a modified FMRP-
81 independent DGKκ transgene provided long-term correction of the cerebral DAG/PA
82 unbalance and of the FXS-related core behavioral phenotypes [28]. These data suggest DGKκ loss
83 contributes centrally to FXS pathomechanisms. However, DGKκ's exact neuronal roles and
84 FMRP's control mechanism remained unknown.
85 Here we identify a previously unrecognized mechanism whereby FMRP regulates DGKκ
86 translation by binding to a unique repeated RNA consensus motif that encodes a hard-to-
87 translate amino acid sequence. We show that m^6A modifications recruit FMRP and its
88 homologs FXRs to resolve ribosome collisions on *Dgkκ* mRNA. In the *Fmr1*-KO brain, we
89 identify region-specific deficits in DGKκ translation and demonstrate that DGKκ loss
90 recapitulates FXS-like phenotypes, including altered neuronal morphology, signaling,
91 behaviors, and physiology, and excessive protein synthesis — a hallmark of the disorder.
92 Moreover, rare missense *DGKk* variants identified in individuals with intellectual
93 developmental disorder support a conserved role in human neurodevelopment. Altogether,

these findings establish FMRP as a positive translational regulator of DGKκ, a master controller of neuronal protein synthesis, thereby resolving a central paradox in FXS pathophysiology.

Results

FMRP binds to RNA sequence that encodes EPAP repeats

Dgkκ mRNA is a primary target of FMRP in primary murine cortical neurons and its expression is severely altered in both *Fmr1*-KO mice and human FXS patients brains [23,28]. Identifying FMRP binding site on its RNA targets could help elucidate the mechanism(s) by which FMRP modulates translation.

DGKκ exhibits low expression levels, which poses challenges for conventional CLIP-seq methods to achieve adequate coverage of this gene. To address this issue, we adopted a HITS-CLIP strategy using a validated FMRP antibody (**Fig. S1A**) in hypothalamic neurons, where *Dgkκ* transcripts are 40-fold more abundant than in cortical neurons (**Fig. S1B**), to enhance sequencing coverage of *Dgkκ* mRNA. The robustness of the HITS-CLIP approach was supported by the detection of a single, well-defined FMRP-binding peak in the GC-rich exon 14 of *Fmr1* (**Fig. S1C**), the initial G-quadruplex–forming region with high affinity for FMRP [27], by the lack of enrichment of housekeeping genes like *Rplp0* mRNA (**Fig. S1C**), and by a significant overlap with previous FMRP-CLIP studies (**Fig. S1D**). Strikingly, a single strong FMRP peak was identified in the *Dgkκ* transcript, located within the coding sequence of exon 1 (**Fig. 1A**). This result was further confirmed using a modified iCLIP method (**Fig. S1E**). The FMRP binding site on *Dgkκ* mRNA spans a ~500-nucleotide region within exon 1, characterized by a high GC content and corresponds to more than 20 conserved repeats, preserved at both the RNA and protein levels, located downstream of a proline-rich region. The repetitive sequences are composed of a conserved GARCCGGCCCCA dodecamer motif (**Fig. 1A**) that encodes EPAP/EPDP amino acid repeats (this RNA sequence is thereafter called

119 "EPAP") (**Fig. S1F**). A reporter mRNA fused to exon 1 of *Dgkκ* was strongly bound by
120 endogenous FMRP in Hela cells compared with a control construct lacking it, while deletion of
121 the EPAP repeats [nt 316-874] abolished the interaction (**Fig. 1B**), confirming that the
122 interaction of FMRP with this sequence is necessary.
123

124 **FMRP binds to "EPAP" RNA sequence in an m6A-dependent manner**

125 A growing number of studies suggest that mRNAs bound by FMRP are enriched in m^6A
126 modifications [9,32,33]. Interestingly, by querying the RMBase database
127 (http://rna.sysu.edu.cn/rmbase), and reanalyzing brain m6A-seq [34], we identified a single strong
128 peak of m^6A RNA modification on *Dgkκ* mRNA, located in exon 1, centered on the EPAP
129 repeats (**Fig. 1A**). This localization contrasts with the typical m^6A distribution, predominantly
130 found around the stop codon or in long internal exons [35], which suggested an alternative
131 function.
132 To determine whether m^6A modifications in *Dgkκ* mRNA are required for FMRP binding, we
133 performed CLIP-qRT-PCR experiments in primary cortical neurons where METTL3, the
134 catalytic component of the METTL3/METTL14 m^6A writer complex [36], was silenced using
135 siRNAs. We confirmed a nearly 50% reduction in METTL3 expression after 72 hours in
136 neurons (**Fig. S1G**) and we assessed its impact on several known FMRP mRNA targets
137 containing m^6A, including *Map1b, Psd95, Cdk5r1,* and *Dgkκ*. We included *Bdnf* (methylated)
138 and *Rplp0* (unmethylated) mRNAs, which are not known FMRP targets, as controls. We
139 observed a significant upregulation of *Psd95* and a trend toward upregulation of *Cdk5r1*and
140 *Bdnf,* as well as for *Dgkκ,* in agreement with the role of m^6A in mRNA decay for those known
141 modified mRNAs [37] (**Fig. S1H**). We then assessed the interaction between FMRP and these
142 mRNAs. As expected *Dgkκ* exhibited a strong CLIP efficiency, in contrast with all tested
143 mRNAs, but strikingly, only *Dgkκ* was affected by METTL3 knockdown (**Fig. 1C**).

144 Specifically, CLIP/Input enrichment decreased by approximately 50% in METTL3 knockdown
145 conditions compared to controls, indicating that FMRP binding to *Dgkκ* mRNA is dependent
146 on m^6A modifications.
147 To investigate whether FMRP binding to the "EPAP" sequence is direct and dependent on m^6A,
148 we analyzed the interaction of purified human FMRP isoform 1, the most abundant isoform,
149 with a 76-nt synthetic RNA sequence containing 7 EPAP repeats bearing or not m^6A. Using
150 EMSA, we confirmed a direct interaction between FMRP and the (EPAP)7 RNA, with a
151 twofold higher affinity for the methylated compared to the unmethylated form (**Fig. S1I**). These
152 findings indicate that FMRP can bind the "EPAP" RNA motif *in vitro* and that its affinity is
153 enhanced by m^6A modifications.
154 m^6A modifications recruit proteins that regulate RNA fate [33,38–41]. Given that these proteins may
155 influence DGKκ translational regulation, we conducted RNA-pulldown proteomic analysis
156 using the (EPAP)7 RNA, with and without m^6As, immobilized on streptavidin beads and
157 incubated with cortical neuronal lysate. Interestingly, we observed enrichment of FMRP, as
158 well as its paralogs FXR1P and FXR2P, with the methylated RNA (**Fig. 1D and**
159 **supplementary Table S1**), consistent with the EMSA results. Additionally, we observed
160 significant enrichment of the m^6A readers YTHDF1, YTHDF3, and to a lesser extent, YTHDF2
161 (**Fig. 1D**). Moreover, the stress granule factor G3BP1 exhibited a preference for the
162 unmethylated RNA, as previously demonstrated [39] (**Fig. 1D**). Analysis of RIP-seq datasets from
163 m^6A readers YTHDF1, YTHDF2, and YTHDF3 in primary hippocampal neurons [42]
164 corroborated our RNA-pulldown results, with YTHDF1 and YTHDF3 showing higher binding
165 affinity for *Dgkκ* mRNA compared to YTHDF2 (**Fig. S1J**). We complemented these data using
166 RNA native hold-up (RNA-nHU), an interactomic method adapted from [43] that enables
167 assessment of the relative binding affinities of an RNA ligand with its protein interactors within
168 cell extracts (**Fig. 1E**). The RNA-nHU experiment was performed using both methylated and

169 unmethylated (EPAP)7 RNA baits at concentrations ranging from 0 to 2.5 μM, incubated with
170 cortical neuronal lysate. First, we confirmed that YTHDF1 exhibits significant affinity for m^6A-
171 containing RNA, which is exclusively dependent on the presence of m^6A (**Fig. 1E**). Consistent
172 with our RNA pulldown proteomics data, we also observed that m^6A modification repels
173 TRA2B binding, resulting in a higher affinity for the unmethylated RNA (**Fig. 1E**). We also
174 confirmed the interaction of FMRP with the unmethylated (EPAP)7 and observed enhanced
175 affinity for the methylated form (**Fig. 1E**). A similar binding was observed with the FXR1P
176 paralog (**Fig. 1E**). The known heterodimerization of FXRs, combined with these findings,
177 suggests that FXRs bind cooperatively to the m^6A-EPAP motif. We therefore used RNA-nHU
178 to investigate whether the absence of FMRP affects FXR1P and FXR2P binding. In *Fmr1*-KO
179 cortical neurons, the interaction between FXR1P and the m^6A-containing (EPAP)7 probe was
180 decreased, suggesting that FXR1P, requires FMRP for a robust interaction with the "EPAP"
181 (**Fig. 1E**).
182

183 **FMRP does not regulate *Dgkκ* mRNA transport and nuclear export**

184 FMRP has been described to modulate neuritic transport and nuclear export of mRNAs [32,44,45].
185 Since m^6A was shown to influence mRNA neuritic transport and FMRP described as an m^6A
186 reader [9,32,33], we assessed whether the loss of FMRP could alter *Dgkκ* mRNA transport into
187 neurites. For this purpose, we used primary cortical neurons grown on filters to physically
188 separate soma from neurites and quantify mRNA levels by qRT-PCR in both fractions. The
189 enrichment of *Col3a1* mRNA in neurites, a previously established transported mRNA, and the
190 enrichment of *Gng3* mRNA in soma, known to be poorly transported, confirmed the quality of
191 preparations (**Fig. S1K**). Our data showed that approximately 50% of *Dgkκ* mRNA is present
192 in neurites, slightly exceeding the level observed for *Psd95* mRNA (~40%). The absence of

193 transport defect in *Fmr1*-KO neurons, indicated that *Dgkκ* mRNA transport into neurites is
194 independent of FMRP (**Fig. S1K**).
195 Then, the nuclear export was assessed by isolating nuclei from the cytosol in WT and *Fmr1*-
196 KO brain samples to quantify mRNA level by qRT-PCR on each fraction. The enrichment of
197 nuclear U2 snRNA in nuclear fraction confirmed the correct separation of nuclei from cytosol.
198 However, we detected no difference in *Dgkκ* mRNA levels between the nuclear and cytosolic
199 fractions, indicating that FMRP does not influence the nuclear export of *Dgkκ* mRNA (**Fig.**
200 **S1L**). These results suggest that FMRP is not involved in the regulation of *Dgkκ* mRNA neurite
201 transport or nuclear export.
202
203 **EPAP repeats induce ribosome stalling**
204 To determine the influence of "EPAP" sequence on DGKκ expression, we first assessed the
205 consequence of the deletion of the exon 1 in *Dgkκ* mRNA (Δex1-DGKκ). Interestingly, deletion
206 of this region resulted in a marked increase in DGKκ protein expression in Hela cells (**Fig. 2A**).
207 Consistently, reporter NLuc construct containing this region (ex1-DGKκ-NLuc) displayed
208 approximately sixfold lower expression than control construct, indicating that this region
209 contains repressive element for DGKκ expression (**Fig. 2B**). "EPAP" RNA sequence encodes
210 ~80% of prolines and acidic amino acids (aspartate D and glutamate E) (**Fig. 1A**), well-
211 established to cause ribosome stalling [46–49], suggesting a ribosomal stalling could be imposed
212 by the protein sequence itself. To test this hypothesis, and to distinguish the contributions of
213 the RNA sequence itself from its role in protein coding, we introduced reading-frame shifts that
214 altered the resulting polypeptide sequence while preserving the overall RNA sequence. As
215 expected, disrupting the proline-rich motif ($fs_{-1}Pro_{+1}$-NLuc) upstream of the EPAP repeats
216 increased NLuc activity, consistent with a relief of peptide-mediated translational repression
217 (**Fig. 2B**). Strikingly, frame shifts at the EPAP repeats ($fs_{-1}EPAP_{+1}$-NLuc, $fs_{+1}EPAP_{-1}$-NLuc)

218 produced a comparable increase in NLuc activity, indicating that both proline-rich and EPAP
219 repeats exert an inhibitory effect primarily through their decoding rather than at their RNA
220 sequence level (**Fig. 2B**). Because impaired translation elongation promotes ribosomal
221 collisions [50], we next investigated whether the "EPAP" promotes such collisions. To this end,
222 we performed RNase protection assays to detect ribosome-protected RNA fragments within the
223 *Dgkκ* exon 1 mRNA sequence. Treatment of cells with a low concentration of the elongation
224 inhibitor emetine, which enhances ribosomal collisions [51], increased the abundance of disomes
225 in RNase A–digested lysates fractionated on a sucrose gradient. (**Fig. 2C**). Accordingly, using
226 a radiolabeled probe targeting the luciferase sequence, we detected disome footprints of ~60 nt
227 upon emetine treatment, in contrast to the ~30 nt monosome footprints observed in control
228 condition (**Fig. 2C**). Strikingly, fusion of the exon 1 of DGKκ upstream the NLuc reporter
229 resulted in a strong depletion of monosome within the luciferase sequence, consistent with a
230 strong translational roadblock (**Fig. 2D**). Moreover, when using an EPAP-specific probe, we
231 detected ribosome footprints corresponding to higher-order collided ribosomes. Importantly,
232 this signal was dependent on the EPAP coding frame: changing the reading frame within the
233 EPAP motif markedly reduced the abundance of higher-order collision footprints relative to
234 monosome footprints (**Fig. 2D**) and slightly increase the downstream monosome signal within
235 the luciferase sequence, thereby excluding a contribution from RNA secondary structure.
236 Together, these data demonstrate that the EPAP-encoding region of *Dgkκ* promotes ribosomal
237 collisions in a reading frame–dependent manner, consistent with a mechanism of translation
238 repression.
239
240 **FMRP alleviates ribosomal stalling imposed by EPAP repeats**
241 To better characterize the mode of action of FMRP in controlling *Dgkκ* mRNA translation, we
242 overexpressed an ex1–DGKκ–NLuc reporter in wild-type and *Fmr1*-KO neurons. Remarkably,

243 we partially recapitulated FMRP-dependent translational control, observing ~40% reduced
244 luciferase activity in *Fmr1*-KO neurons (**Fig. 2E**). Deleting the EPAP repeats abolished this
245 regulation. Likewise, frameshift mutations in the EPAP repeats (−1/+1 and +1/−1), which
246 preserve the RNA sequence but alter the encoded protein, eliminated FMRP-dependent control
247 (**Fig. 2E**). Changing the reading frame within the proline-rich sequence similarly disrupted
248 regulation, demonstrating that the encoded protein sequence–rather than the RNA sequence
249 itself–is essential for FMRP-mediated translational enhancement (**Fig. 2E**).
250 Together, these data reveal that FMRP promotes context-dependent translation at sequences
251 encoding repetitive, sub-optimal amino acids.
252
253 **m^{6}A enhances translation efficiency within the EPAP repeat context**
254 The conserved m^{6}A consensus motif within the EPAP domain in both mouse *Dgkκ* and human
255 *DGKκ* corresponds to the GA**A**CCN context encoding the E-P dipeptide, with methylation
256 occurring on the GA**A** codon. Recent studies indicate that m^{6}A modifications within coding
257 sequences, particularly on GA**A** codon, slow translation elongation and ultimately trigger
258 ribosomal collisions [52–54].
259 To investigate the impact of EPAP repeats on DGKκ expression, we used the nanoluciferase
260 gene reporter system described above in non-neuronal cells. Cells were treated with *METTL3*
261 siRNA which resulted in a ~2.5-fold increase in ex1-DGKκ-NLuc RNA levels, markedly higher
262 than that observed for the control NLuc construct (**Fig. S2A**). Notably, this increased RNA
263 level was specific to the EPAP repeats, as its deletion in the ΔEPAP-NLuc construct, abolished
264 this effect (**Fig. S2A**). These results are consistent with previous studies showing that m^{6}A
265 modifications within the coding sequence promote efficient mRNA degradation [55].
266 Surprisingly, however, luciferase activity from the ex1-DGKκ-NLuc construct did not correlate
267 with RNA abundance, leading to an ~80% reduction in translation efficiency (luciferase/RNA

268 ratio) when silencing METTL3 compared with the control condition (**Fig. 2F**). This effect was
269 also seen, in a dose-dependent manner using STM2457 METTL3 specific inhibitor (**Fig. S2B**).
270 Interestingly, this effect that was not observed when the EPAP repeats or the proline-rich region
271 were out of frame (**Fig. 2F**) and led to an increase or no change of translation efficiency in
272 accordance with previous reports [53,54,56,57] .
273 Moreover, this effect is independent of YTHDF1 and YTHDF2, as their silencing increased
274 RNA level of ex1-DGKκ-NLuc construct, without affecting its translation efficiency, consistent
275 with their well-established roles in regulating mRNA stability [35] (**Fig. S2C**).
276 Overall, these results indicate that, within the EPAP repeat context, m^6A modifications
277 counteract a sequence-imposed translational repression and positively modulate translation
278 efficiency.
279
280 **DGKκ deficit varies across brain despite conserved *Dgkκ* mRNA/FMRP interaction**
281 Our prior work showed that FMRP loss strongly impairs DGKk translation in *Fmr1*-KO cortical
282 neurons [23,28]. Given DGKk's heterogeneous brain expression (**Fig. 3A**), neuron-specificity (**Fig.**
283 **3B**), and binding by all FXR paralogs to the EPAP repeats (**Fig. 1D**), we investigated whether
284 the expression of DGKk was differentially altered across distinct brain regions.
285 Detection of DGKκ by conventional methods is challenging due to its low protein abundance
286 and the absence of specific commercial antibodies. To assess the consequence of FMRP loss
287 on DGKκ protein level, we used targeted mass spectrometry called Parallel Reaction
288 Monitoring combined with stable isotope-labeled standard peptides (PRM-SIS) to assess DGKκ
289 absolute level. While there was no difference in *Dgkκ* mRNA level between *Fmr1*-KO and WT
290 across the brain (**Fig. 3C**), DGKκ protein was reduced by ~80% in *Fmr1*-KO cortex and
291 primary cortical neurons, contrasting with a ~50% decrease in the hypothalamus (where DGKκ
292 is most highly expressed) (**Fig. 3D, Fig. S3A, B**). This observation prompted us to determine

293 whether the interaction between FMRP and *Dgkκ* mRNA was conserved across different brain
294 regions. Thus, using a CLIP approach to compare FMRP interaction in cortical neurons, where
295 DGKκ expression is very low, to hypothalamic neurons, where *Dgkκ* is over 40-fold higher
296 (**Fig. 3C**). Surprisingly, CLIP-qRT-PCR analyses revealed a strong and similar enrichment of
297 *Dgkκ* mRNA relative to input similar in both neuron subtypes (**Fig. 3E**, **F**). This suggests that
298 *Dgkκ* mRNA is a favored target of FMRP compared with other proposed targets such as *Map1b*
299 and *Psd95,* across different brain regions and independently of its mRNA level.
300 The FXR paralogs (FMRP, FXR1, FXR2) share ~65% sequence homology across mammals,
301 including conserved KH1, KH2, and RGG RNA-binding domains [58], suggesting functional
302 redundancy. *Fmr1* mRNA level was found ~4-fold higher in cortex than hypothalamus, whereas
303 *Fxr1* showed the inverse pattern (**Fig. S3C**), suggesting that FXRs may display reciprocal
304 expression across brain regions. These differences persisted at the protein level, with opposing
305 FMRP/FXR1 abundance profiles (**Fig. 3G**). To test whether FXR1P binds and regulates *Dgkκ*
306 mRNA we performed CLIP-FXR1P in primary hypothalamic neurons where *Dgkκ* expression
307 peaks. *cMyc* mRNA – a known FXR1P target [59] – was significantly enriched relative to input,
308 IgG, and negative control *Rplp0*. *Dgkκ* mRNA showed 5- to 10-fold greater enrichment than
309 all tested targets, including *Map1b*, *cMyc*, and *Psd95* (**Fig. 3H**), confirming the specific and
310 strong binding of FXR1P to *Dgkκ* mRNA.
311 These data suggest a compensatory mechanism by FXR paralogs in DGKκ-rich regions that
312 may account for the partial loss of DGKκ protein levels in *Fmr1*-KO mice.
313

314 ***Dgkκ*-KO mouse recapitulates core FXS behavioral phenotypes**

315 To assess the biological role of DGKκ, we generated a *Dgkκ* knockout mouse (*Dgkκ*-KO) via
316 CRISPR-Cas9 deletion of exon 8, inducing a frameshift and premature stop in exon 9 (**Fig.**
317 **S4A-D**). No transcriptional compensation occurred among the nine other DGK isoforms (**Fig.**

318 **S4E**). *Dgkκ*-KO mice appeared grossly normal, with no reproductive bias or congenital
319 malformation–including absence of hypospadias, in contrast to previous proposal based on
320 GWAS [60]. *Dgkκ*-KO mice exhibited progressive body weight gain from 3-22 weeks (**Fig. 4A**),
321 driven by lean mass (**Fig. 4B**) and fluid increases (**Fig. 4C**)—not fat (**Fig. 4D**) or size (qNMR;
322 **Fig. 4E**)—plus elevated bone density (**Fig. 4F**), heart weight (**Fig. 4GH),** and compensated
323 cardiomyopathy (**Fig. S4FG**). Unlike *Fmr1*-KO mice and FXS patients, macroorchidism was
324 absent [11,61]. Thus, DGKκ loss recapitulates syndromic FXS-like overgrowth [62], while other
325 FMRP targets likely mediate macroorchidism.
326 At 13 weeks, *Dgkκ*-KO male mice underwent a battery of behavioral and cognitive tests. Use
327 of open field test revealed an increased locomotor activity of *Dgkκ*-KO compared to WT mice
328 (**Fig. 4I**) with increased time spent in the center of the arena (**Fig. 4J**) that were evocative of a
329 hyperactivity behavior with reduced anxiety. Hyperactivity was also supported by the increased
330 marble burying (**Fig. 4K**). Increased digging duration and number of diggings suggested
331 compulsive-like behavior (**Fig. 4L**). An increased contact numbers and duration in the social
332 interaction test suggested increased sociability (**Fig. 4M, Fig. S4H**), but could also resulted
333 from hyperactivity and reduced anxiety. Increased time in the open arm in the elevated plus
334 maze with increased arm entries trends suggested also hyperactivity and reduced anxiety (**Fig.**
335 **4N, Fig. S4I**). A trend for alteration of recognition ability was observed in the novel object
336 recognition test (**Fig. S4J**), suggesting *Dgkκ*-KO mice do not present major episodic-like
337 memory alteration. No nesting behavior or social memory defects were detected (**Fig. S4KL).**
338 Finally, the startle response amplitude after pre-pulse Inhibition (PPI) was also found
339 significantly increased (**Fig. 4O**), suggesting that *Dgkκ*-KO mice have a sensorimotor gating
340 deficit and a hypersensitivity to acoustic stimuli. Collectively, these findings underscore the
341 impact of DGKκ loss on multiple aspects of mouse cognitive and behavioral function, including
342 hyperactivity, hypersensitivity, and compulsive-like behaviors, highlighting its role in

343 neurodevelopment. Notably, these phenotypes overlap with those observed in the *Fmr1*-KO
344 mouse model.
345
346 **DGKκ loss disrupts spine morphology, mGluRI-dependent activity, and leads to**
347 **excessive neuronal translation**
348 The neuron-specific expression of DGKκ (**Fig 3B**) and the neurodevelopmental behavioral
349 alterations caused by its depletion suggested that DGKκ plays important neuronal functions. To
350 identify the neuronal subcellular localization of DGKκ, we conducted an overexpression
351 experiment in primary hippocampal neurons and performed immunostaining against HA-
352 tagged DGKκ at DIV17. DGKκ was predominantly found enriched at the plasma membrane,
353 similar to when it was overexpressed in non-neuronal cells [63]. Within dendrites, DGKκ was
354 found specifically enriched in post-synaptic densities of mature spines colocalizing with the
355 synaptic marker PSD95 (**Fig. 5A**) and ribopuromycylation signal (**Fig. 5B and S5A**). This
356 finding supports a role of DGKκ in synaptic function and suggests a contribution in modulating
357 dendritic spines local translation.
358 Dendritic spine morphology is frequently altered in neurodevelopmental disorders and these
359 morphological alterations are proposed as an underlying cause of these disorders [64]. To analyze
360 the effects of DGKκ loss on dendritic spine morphology, primary hippocampal neurons from
361 WT and *Dgkκ*-KO mice were magnetofected at 4DIV with a GFP-expressing plasmid and
362 imaged at DIV21. A significant decrease in mature "stubby" and "mushroom" spines alongside
363 a notable increase in immature "long thin" and "filopodia" spines was observed in *Dgkκ*-KO
364 neurons (**Fig. 5C**).
365 Given the cognitive alterations of *Dgkκ*-KO mice, the increased proportion of immature spines
366 in *Dgkκ*-KO neurons, and the consequences of other DGKs loss on synaptic plasticity [65], we
367 hypothesized that the loss of DGKκ would likely lead to synaptic transmission dysfunction. To

368 test this hypothesis, we recorded the neuronal activity of WT and *Dgkκ*-KO primary cortical
369 neurons at DIV21 (time at which neural activity was highest **Fig. S5B**)
370 on high-density multi-electrode array (HD-MEA) chips. The maturity of the culture was
371 assessed by the spiking frequency of individual neurons, the burst neuronal network activity
372 (**Fig. S5C**), and the responsiveness to (S)-3,5-Dihydroxyphenylglycine (DHPG), a specific
373 agonist of group 1 metabotropic glutamate receptors (mGluRIs) (**Fig. 5D**).
374 While the number of active units was consistent between WT and *Dgkκ*-KO neurons, reflecting
375 a comparable number of cells on the HD-MEA chip, at basal level, we observed similar firing
376 rates and burst network frequencies between WT and *Dgkκ*-KO neurons, suggesting no
377 apparent difference in absence of stimuli (**Fig. 5D**). However, upon neuronal activation with
378 DHPG, we observed a 5-fold increase in neuronal firing rate for WT neurons, compared to only
379 a 3-fold increase for *Dgkκ*-KO neurons. Furthermore, WT neurons showed an increased
380 synchronization of their network activity whereas *Dgkκ*-KO neurons showed a loss of
381 synchronization (**Fig. 5D**). Overall, the absence of DGKκ in neurons disrupts their intrinsic
382 firing activity and synaptic transmission, resulting in alterations to the neuronal network
383 coherence in vitro.
384 DGKs convert DAG into PA and are thought to play a key role in neuronal signaling by
385 attenuating DAG-mediated pathways [65]. To define the molecular alterations caused by the loss
386 of DGKκ, we analyzed the activation status of several members of the DAG-activated pathways
387 in cortical neurons. PKC, a main direct effector of DAG was found overactivated (**Fig. 5E**), in
388 agreement with an excess of DAG signaling. Analysis of several other downstream effectors
389 revealed that AKT, S6, and eIF4E were also overactivated, further supporting the alteration of
390 DAG signaling. S6 and eIF4E are final effectors of DAG-mediated pathways, their
391 phosphorylation levels in the brain are associated with enhanced protein synthesis rate [66,67].
392 Concordantly, neuronal translation rate was found to be increased in *Dgkκ*-KO cortical neurons

393 by puromycin incorporation assay (**Fig. 5F**). We further confirmed that DAG pathway was
394 altered in hypothalamic primary neurons, as DGKκ is expressed at a much higher level in this
395 neuronal type (**Fig. S5D**).
396 Thus, DGKκ loss phenocopies *Fmr1* KO spine/translation defects through mGluRI-DAG
397 pathway overdrive.
398

399 **Rare missense variants in *DGKk* identified in individuals with neurodevelopmental**
400 **disorders affect DGKk localization**

401 Given the cognitive and behavioral alterations observed in the *Dgkκ*-KO mice, we investigated
402 whether *DGKk* might contribute to neurodevelopmental disorders (NDD) in humans. To
403 address this, we searched rare non-synonymous variants identified in NDD patients through
404 Genematcher. We retrieved three hemizygous missense variants—p.(Thr282Ile),
405 p.(Lys526Asn), and p.(Arg584Cys)—each detected in males with NDD who lacked other
406 pathogenic variants in genomic analyses (exome or genome sequencing)- affecting conserved
407 amino acids and absent from the gnomAD general population database (gnomAD v4.1.0). To
408 assess their potential deleterious impact on protein function, we designed a functional assay.
409 As controls, we included two presumably benign missense variants—p.(Ile612Asn) and
410 p.(Arg851Cys)—reported in 1,079 and 1,065 hemizygous males in gnomAD, respectively, and
411 the two catalytically inactive DGKk mutant, deleted from the C1 (DAG binding domain) or
412 C4a (catalytic domain) domains [63].
413 To determine the functional impact of DGKk variants, we assesed the expression level and
414 localization of DGKk p.(Thr282Ile), p.(Lys526Asn), and p.(Arg584Cys) variants (**Fig. S6A**) in
415 neuronal and non-neuronal cells. The overexpression in HeLa cells of the variants did not lead
416 to an altered protein level compared to WT and benign DGKk variants (**Fig. S6B**). However,
417 compared to WT and benign variants, both DGKk p.(Thr282Ile) and p.(Arg584Cys) variants

418 failed to localize at the plasma membrane in HeLa cells, similarly to C1 and C4a deletion
419 mutants (**Fig. S6C**). In neurons, WT and non-pathologic DGKk variants localized at the plasma
420 membrane of cell body as well as in dendrites. Compared to WT and benign variants,
421 p.(Thr282Ile) and p.(Arg584Cys) and DGKk deletion mutants failed to localize efficiently in
422 dendrites, suggesting they have an altered neuronal function (**Fig. S6D**). Further, experiments
423 will be required to assess the pathogenicity of p.(Lys526Asn) variant.
424 Thus, DGKk rare loss-of-function variants identified in patients with neurodevelopmental
425 disorders impair DGKk function in both neuronal and non-neuronal cells, thereby strengthening
426 the candidacy of DGKk as a novel contributor to neurodevelopmental disorders in humans.
427

428 **Discussion**

429 The identification of the RNA binding properties of FMRP has been a long-standing question
430 in the field of FXS research. In addition to its high affinity for highly structured RNA [22,26,27],
431 FMRP has also been shown to have affinity with short abundant RNA sequences [24,25,68,69]. The
432 FMRP binding motif "EPAP" identified here is distinct from previously described motifs and
433 consists of a tandemly repeated GARCCGGCCCCA (more than 20 repeats) dodecamer
434 containing a high density of m^6A modifications. To our knowledge, FMRP displays for *Dgkκ*
435 mRNA the best reported binding affinity [23]. Our data suggest that FMRP's unprecedented
436 affinity for *Dgkκ* mRNA can be driven by the sequence of the motif itself, its repetitive nature,
437 its high density of m^6A modifications, and its collaborative interaction with FMRP paralogs.
438 The "EPAP" RNA motif encodes a conserved, highly repetitive sequence (~120 amino acids),
439 composed of ~80% acidic residues (E, D) and prolines, located immediately downstream of a
440 proline stretch (**Fig. 1A**). This motif resides in exon 1, which encodes N-terminal region of
441 DGKκ with no apparent role in catalytic function [28,63], implying strong selective pressure to
442 maintain its in-frame conservation. The proline stretch upstream of the EPAP repeats, well

443 established ribosome stalling element [46], is necessary to induce ribosome stalling events. The
444 EPAP repeats are necessary to recruit FMRP in a m^6A dependent manner in order to increase
445 translation efficiency of DGKκ in neurons (**Fig. 2B,E,F**; **Fig. S6D**). Our findings highlight a
446 nuanced role of FMRP that extends beyond its canonical function as a translational repressor,
447 consistent with both a study in *Drosophila* showing that FMRP enhances translation of large
448 proteins [70] and studies showing that FMRP associates with sequences where ribosomes pause
449 — enriched in glutamate and aspartate— without directly establishing the stalling [71,72]. Further
450 analysis of our CLIP-seq data revealed that FMRP binding events occur on sequences encoding
451 repeated amino acids known to promote ribosome stalling (**Fig. S7A, B**). The EPAP motif is
452 among the motifs with highest proportion of such amino acids and the one with the greatest
453 number of m6A consensus sites (**Fig. S7C**).
454 An activation of translation induced by the combined action of two factors, FMRP and m^6A,
455 both well described as translation repressors [7,53,54,56,57], seems paradoxical. Yet, ribosome
456 pausing induced by m^6A in coding sequence has been shown to be beneficial for the translation
457 of certain transcripts [52]. A similar mechanism may be at play in the stall-prone Pro-EPAP
458 sequence, where the FMRP/m6A-mediated slowdown of translation may be beneficial to
459 locally mitigating ribosomal collisions, ultimately enhancing productive translation (**Fig. S7D**).
460 In this framework, FMRP emerges not simply as a brake on protein synthesis, but as a regulator
461 of translational flow, fine-tuning ribosome behavior to modulate the expression of
462 neurodevelopmental effectors in response to the intrinsic properties of the coding sequence.
463 Further studies will be required to determine how FMRP regulates ribosomal collisions, either
464 in opposition to or in concert with quality control factors such as ZNF598 or ASCC3 that
465 intervene to rescue ribosome collision events [73–75] and recent work showed that this could be
466 exploited to ameliorate FXS *Fmr1*-KO phenotypes [76]. Moreover, it will be mechanistically

467 insightful to define the mode of action of FMRP through structural studies of FMRP in complex
468 with the ribosome bound to the EPAP motif, with or without m^6A modification.
469
470 We identified differential DGKκ level alterations across the *Fmr1*-KO brain, revealing potential
471 compensation by the FMRP paralog FXR1P, which exhibits mirror-inversed expression relative
472 to FMRP across brain regions. This reciprocal pattern suggests functional overlap among FXR
473 proteins and correlation of *Fmr1*-KO phenotypes with regionally specific DGKκ reductions
474 (~80% in the cortex and ~50% in the hypothalamus).

475 Despite a low and restricted expression in certain brain areas, the loss of DGKκ revealed both
476 neuronal and non-neuronal phenotypes shared with the *Fmr1*-KO model (**Table 1**). At
477 behavioral level, the *Dgkκ*-KO model exhibits significant neurodevelopmental impairments,
478 notably marked hyperactivity, reduced anxiety, hypersensitivity, and compulsive behavior,
479 which are recurrent phenotypes of the *Fmr1*-KO mice [77]. Consistently with other DGK mouse
480 models [78–80], these findings confirm the importance of DAG-associated lipid signaling in
481 neurodevelopment. The identification of two rare missense *DGKk* variants in males with
482 neurodevelopmental phenotype, which disrupt DGKκ protein neuronal localization (**Fig. S6D**),
483 positions *DGKκ* as a novel NDD candidate. Additional patients harboring deleterious variants
484 will be required to confirm its role in NDD.

485 *Dgkκ*-KO analysis revealed the functional importance of the DGKκ enzyme in regulating
486 neuronal DAG-signaling — a mechanism central to the adaptation to external stimuli in many
487 cell types [81–84]— and how FMRP contributes to its regulation. The balance of DAG and PA
488 plays a pivotal role in intracellular signaling [82] and its dysregulation, as a consequence of DGKκ
489 lack of expression, has been postulated as an underlying pathomechanism of FXS [23,30]. *Dgkκ*-
490 KO neurons exhibit exacerbated DAG-signaling pathways associated with a global increase of

491 neuronal protein synthesis rate. Increased neuronal translation rate is considered a hallmark of
492 FXS condition and is proposed to underly LTP/LTD defects along with abnormal dendritic
493 spine morphology leading to synaptic defects and some behavioral alterations [12]. The exact
494 cause of neuronal translation increase in FXS was unclear and hypothesized to be a consequence
495 of the loss of repression by FMRP acting individually on its multiple targets [12]. Our data
496 unambigously demonstrate that the loss of DGKκ alone leads to such an effect. The loss of
497 DGKκ leads also to abnormal dendritic spine morphology and an impaired mGlurI-dependent
498 neuronal activity, similarly to the *Fmr1*-KO model. These data suggest that DGKκ loss by itself
499 contributes to a large body of neuronal defects of FXS condition.

500 Beside the central nervous system phenotypes, several physiological alterations have been
501 reported in *Fmr1*-KO mice, including lipids and glucose metabolism defects associated with
502 increased non-fat body mass, increased muscle mass and global skeleton length, evocative of
503 an overgrowth phenotype [62,85]. These features are present in a proportion of FXS patients [62,86].
504 FMRP was proposed to impact the hormonal system and notably hypothalamic function, which
505 could explain the non-neuronal phenotypes in FXS [86–90].
506 To date, the molecular origin of this phenotype remains unknown. Remarkably, *Dgkκ*-KO mice
507 mirror—and even exaggerate— the overgrowth phenotype observed in *Fmr1*-KO mice.
508 DGKκ's peak hypothalamic expression, coupled with its ~50% reduction in *Fmr1*-KO mice,
509 makes DGKκ a relevant candidate mediator of the hypothalamic phenotypes. In this context,
510 Snord116 snoRNA, whose loss causes Prader–Willi syndrome (PWS) [91–93], directly targets
511 *Dgkκ* mRNA [94], and its absence in PWS is associated with DGKκ upregulation [95]. Notably,
512 many PWS phenotypes arise from hypothalamic dysfunction, including hyperphagia, delayed
513 puberty, and short stature, some of which overlap with FXS features [87]. These observations,
514 together with the hypothalamic expression of DGKκ, position it at the crossroads of both
515 disorders, potentially contributing to their contrasting phenotypic traits.

516

517 Together, these findings position DGKκ as a key translational effector of FMRP dysfunction in
518 FXS, opening avenues for targeted therapeutic strategies, such as DGKκ-based AAV
519 approaches or pharmacological agents that modulate DAG/PA levels.
520
521
522 **Material and methods**
523 **Animal model**
524 *Dgkκ*$^{em1(IMPC)Ics}$ (*Dgkκ*-KO) in C57BL/6NCrl background was obtained through Infrafrontier-
525 I3 program by CRISPR/Cas9 deletion of exon 8 (GRCm38.p4 6897240/6897601, details
526 available on www.mousephenotype.org. B6.129P2-Fmr1tm1.2Cidz/J (*Fmr1*-KO) in C57BL/6J
527 was kindly given by Dr Rob Willemsen [61]. Males from the same genotype (thereafter called
528 *Dgkκ*-KO, *Dgkκ*-WT, *Fmr1*-KO, *Fmr1*-WT) were grouped by 3 or 4 individuals at weaning
529 age (4 weeks), in individually ventilated cages (GM500, Tecniplast, UK), with poplar shaving
530 bedding (Lignocell Select, JRS, Germany), and maintained under standard conditions on a 12-
531 h light/dark cycle (7 h/19 h) with standard diet food (standard diet D04, Scientific Animal Food
532 and Engineering, France) and water available ad libitum. Mice from the same cage received the
533 same treatment and were transferred in the phenotyping area the next week. Animal work
534 involved in this study was conducted according to ARRIVE guidelines and received
535 authorization from relevant national committee (Comité National de Reflexion Ethique en
536 Experimentation Animale) with APAFIS #17544-2018111516571205 v7 at the ICS mouse
537 facility (Illkirch, France). Every procedure on mice was performed to ensure that discomfort,
538 distress, pain, and injury would be minimal.
539
540 **Genotyping**
541 Genotyping of *Dgkκ*-KO model was performed after birth on tail genomic DNA by PCR using
542 primers CCTTCAGCAGCCTACCAACATTG and CTTCCGAAGGAACATTCCTTGG
543 producing a 334 amplicon in WT and no product in KO, primers
544 CCAAGGAATGTTCCTTCGGAAG and GAACATGCCCATACTCATGTACCC producing
545 a 288 bp amplicon in WT and no product in KO, and primers
546 CCTTCAGCAGCCTACCAACATTG and GAACATGCCCATACTCATGTACCC
547 producing a 241 bp amplicon in KO and no product in WT. Genotyping of *Fmr1*-KO model
548 was performed as in [28].

549

550 **Behavioral experiments**

551 Behavioral experiments were conducted at 10 weeks. The behavioral experiments were
552 performed under experimenter-independent conditions or by experimenters naive to the
553 treatment conditions. Individual cohorts of male littermate animals (issued from *Dgkκ*$^{y/+}$ x
554 *Dgkκ*$^{+/-}$ mating) were composed of WT and *Dgkκ*-KO subgroups.

555

556 **Elevated plus maze**

557 The apparatus used is automated and made of PVC (Imetronic, Pessac, France). Two open arms
558 (30 Å~ 5 cm) opposite one to the other and crossed by two closed arms (30 Å~ 5 Å~ 15 cm).
559 The maze has infrared captors allowing the detection of mice in the closed arms and different
560 areas of the open arms. The mice were tested during 5 min. The number of entries and time
561 spent in the open arms were measured to calculate an index of anxiety.

562

563 **Nest building**

564 On the day of test, mice were singly transferred in a standard cage for the duration of nest
565 building measurement. A block of nesting material (5 Å~ 5 cm hemp square, Happi Mats,
566 Utopia) was placed in the cage. Pictures were taken and visual scoring occurred at 2, 5, 24 h
567 without disturbing the animals. The room temperature was noted when the nest was scored
568 since nest building has a thermoregulatory function and therefore may be influenced by ambient
569 temperatures. We used a 0-5 scale described by [96]: 0 = undisturbed nesting material; 1 =
570 disturbed nesting material but no nest site; 2 = a flat nest without walls; 3 = a cup nest with a
571 wall less than the height of a dome that would cover a mouse; 4 = an incomplete dome with a
572 wall of the height of a dome; 5 = a complete dome with walls taller than the height of a dome,
573 which may or may not fully enclose the nest.

574

575 **Marble burying**

576 Twenty glass marbles were placed equidistant from each other on the litter of the cages. The
577 mice were left in contact with the marbles for a total period of 30 min. The test was terminated
578 by removing the mice from the cages. The number of marbles was counted after 30 min. A
579 marble was considered buried when two-thirds or more of it was covered with burying
580 substrate.

581

582 **Novel object recognition task**

583 Mice were tested in a circular arena (50 cm diameter and 30 cm height basin). The locomotor
584 activity was recorded with the EthoVision XT video tracking system (Noldus, Wageningen,
585 Netherlands). The arena was homogeneously illuminated (40 Lux) divided into central and
586 peripheral regions. First, animals were habituated to the arena for 15 min. Each mouse was
587 placed in the periphery of the arena and allowed to explore the apparatus. Experimenter were
588 out of the sight of the tested animal. During the test session, the distance traveled and time spent
589 in the central and peripheral regions were recorded. The percentage of time spent in center area
590 was used as index of anxiety. The following day, mice were tested for object recognition in the
591 same arena. Mice were tested for a 10-min acquisition during which they were placed in the
592 arena in presence of a sample objects (2.5 cm diameter marble or 2 cm edge plastic dice). The
593 time took by the animal to explore the samples was manually recorded. The following day, a
594 10-min retention trial was conducted. During this retention trial, the samples A and another
595 object B (marble or dice depending on acquisition) were placed in the open field. The times
596 took to explore the object A and object B by the animal were recorded. A recognition index
597 was calculated as (tB / [tA + tB]) x100.
598
599 **Social recognition test**
600 Social recognition test evaluates the preference of a mouse for a congener as compared to an
601 object placed in an opposite compartment. This test is also used for evaluation of social memory
602 by measuring exploration of a novel congener as compared to a familiar one. The apparatus is
603 a transparent cage composed with a central starting compartment and two side compartments
604 where circular grid cup (goal box) is placed at each extremity, and where the congener can be
605 placed during testing. Testing was performed for two consecutive days. On the first day, the
606 mouse was placed in central box then allowed to explore freely the apparatus for 10 min to
607 attenuate their emotionality. On the second day, a C57BL/6NCrl congener from the same sex
608 was placed in one goal box and an object was placed in the opposite one. The mouse was then
609 placed in the starting central compartment and allowed to explore freely the apparatus for 10
610 min. The position of the congener and object boxes was counterbalanced to avoid any potential
611 spatial preference. The duration of exploration of each goal box (when the mouse is sniffing
612 the grid delimiting the goal box) was manually measured and the percentage of time the mouse
613 took to explore the congener was used as index of social preference (recognition preference).
614 A 10-min retention trial was then performed during which the object was replaced by a novel
615 congener. The duration of exploration of each goal box was manually measured and the

616 percentage of time the mouse takes to explore the congener was used as index of social memory.
617 The social preference index (SR) is defined as (time Congener / [time Object + time
618 Congener])x100; and the social memory index as (time novel Congener / [familiar congener +
619 time novel Congener])x100.
620
621 **PRM-based quantification of DGKκ in tissues**
622 Skyline software was used for the *in-silico* identification of signature peptides based on the
623 following criteria: peptide length of 7 to 25 amino acids, excluding the first 25 N-terminal
624 residues that could potentially constitute a signal peptide; peptides must be unique to the protein
625 of interest (proteotypic); avoid peptides containing Cys (tends to form disulfide bonds), Met
626 (prone to oxidation), Arg-Pro/Lys-Pro (promote missed cleavages), Asn-X-Thr/Asn-X-Ser
627 (sites of N-glycosylation). It is important to select target peptides that are not affected by
628 uncontrolled modifications since these lead to changes in the molecular weight of the peptide,
629 which would appear in two forms and could no longer be considered a signature peptide. A list
630 of mouse DGKκ peptides that meet these requirements was generated and spectral matches
631 were found in the predictive library Prosit. Prosit was built using a deep learning algorithm that
632 was trained with mass spectra obtained from MS analysis of synthetic reference peptides [97].
633 However, experimental spectra for the signature DGKκ peptides were not found in proteomics
634 databases (NIST, GPM, PeptideAtlas), so they needed to be validated empirically. We designed
635 and identified on Skyline software two theoretical DGKκ -specific peptides (P06 and P07). This
636 strategy required validation of the selected peptides and prior information such as elution time,
637 m/z value, charge state, and fragmentation conditions, which is obtained during preliminary
638 measurements by a global acquisition method (DDA) of the target protein produced in an
639 overexpression system [98]. The target peptides are then synthesized chemically with heavy
640 isotopes that incorporate 13C- and 15N-labeled C-terminal arginine (R) or lysine (K), identical
641 in sequence and physicochemical properties to the peptides of interest, that are needed for the
642 actual spiking and quantification of the samples. To improve the precision of absolute
643 abundance measurements, an external calibration curve is produced by measuring the signal
644 intensity of the reference peptides at multiple concentration points. Spike-in of samples with
645 heavy-labeled peptides is used as internal standards.
646
647 Frozen cell pellets or tissues were lysed in RIPA lysis buffer [50 mM Tris-HCl pH 7.4, 0.08
648 mM CaCl2, 100 mM KCl, 1 mM MgCl2, 1% (v/v) NP-40, 0.5% (m/v) sodium deoxycholate,

649 1% (m/v) SDS, 1× complete EDTA-free protease inhibitor cocktail] and protein concentration
650 was determined using Bradford method (Bio-Rad protein assay dye reagent, #5000006). A total
651 of 20 µg of protein extracts were migrated for 15 minutes at 150 V on a 10 % SDS-PAGE gel.
652 Subsequently, the gel was fixed for 30 minutes in a solution containing 10% (v/v) acetic acid
653 and 40% (v/v) ethanol, followed by staining with PageBlue Protein Staining Solution
654 (ThermoScientific) for 1 hour. After multiple washes with ultrapure water, a band
655 corresponding to the expected molecular weight of DGKκ was excised. Gel strips were
656 transferred to a 96-well microplate and de-stained by washing three times with 50 mM
657 ammonium bicarbonate (Sigma) and 50% (v/v) acetonitrile (Biosolve) for 10 minutes at room
658 temperature with agitation at 850 rpm, followed by a wash with 100% acetonitrile under the
659 same conditions. The gel bands were then reduced with 10 mM DTT for 30 minutes at 56°C,
660 followed by alkylation with 50 mM IAA for 30 minutes in the dark. Gel strips were washed
661 again using the same procedure and dried in a SpeedVac for 15 minutes.
662 Digestion was performed overnight at 37°C using trypsin at a concentration of 10 ng/µl diluted
663 in 10% (v/v) acetonitrile, 50 mM ammonium bicarbonate, and 2 mM CaCl2. Peptides were
664 extracted first with 0.2% (v/v) formic acid and 50% (v/v) acetonitrile for 15 minutes at room
665 temperature with agitation at 850 rpm, followed by extraction with 0.2% (v/v) formic acid and
666 90% (v/v) acetonitrile using the same conditions, pooling two gel bands per condition. Finally,
667 the peptide mixture was dried in a SpeedVac for approximately 3 hours, resuspended in 20 µl
668 of 0.1% (v/v) trifluoroacetic acid (TFA), and 0.5 µl was injected into the mass spectrometer.
669
670 **Neuronal primary culture**
671 Cortices, hippocampi, or hypothalami from *Fmr1*-WT, *Fmr1*-KO, *Dgkκ*-WT, or *Dgkκ*-KO
672 E17.5 mouse embryos were dissected in dissection buffer containing 1xPBS, 2.56 mg/mL D-
673 glucose, 3 mg/mL BSA, and 1.16 mM MgSO4. Each brain tissue was then incubated for 25
674 minutes in 100 µL of dissociation buffer composed of Neurobasal medium (GIBCO), 20 U/mL
675 papain (Worthington), and 1 mg/mL DNase I. After centrifugation at 1000 × g for 5 minutes,
676 the dissociation solution was discarded, and 500 µL of ovomucoid (Worthington) inhibitory
677 solution was added and incubated for 6-7 minutes. Following this incubation, the ovomucoid
678 solution was removed, and the cells were gently mechanically dissociated by pipetting 15 times
679 to achieve a single-cell suspension. The dissociated cells were plated on poly-L-lysine
680 hydrobromide-coated (P9155, Sigma) culture plates and cultured for 8 to 21 days in Neurobasal
681 Medium supplemented with B27, penicillin/streptomycin, and 0.5 µM L-glutamine. Half of the

682 media were changed every 2-3 days. For experiments requiring puromycin treatment, cultures
683 were treated with puromycin solution at specified concentrations and durations as indicated.
684
685 **Western-blot**
686 The cell lysates in the Laemmli buffer blue were heated for 5 minutes at 95°C, and 8 µL
687 (equivalent to 15 µg of total protein) were loaded onto an SDS-PAGE denaturing gel composed
688 of a stacking gel [4% (w/v) acrylamide/bisacrylamide 29:1 (v/v); 0.1 M Tris-HCl pH 6.8; 0.1%
689 (w/v) SDS; 0.1% (w/v) APS; 0.01% (w/v) TEMED] and a resolving gel [10% (w/v)
690 acrylamide/bisacrylamide 29:1 (v/v); 0.375 M Tris-HCl pH 8.8; 0.1% (w/v) SDS; 0.1% (w/v)
691 APS; 0.01% (w/v) TEMED]. A molecular weight marker (PageRuler™ Plus Prestained Protein
692 Ladder) was also loaded. The gel was run at 150 V for 1 hour in Tris/Glycine/SDS running
693 buffer [0.001 M Tris-HCl; 0.2 M Glycine; 0.1% (w/v) SDS]. The transfer was performed onto
694 a PVDF membrane (0.22 µM, Millipore) activated for 5 minutes in 100% ethanol, for 1.5 hours
695 at 200 mA in Tris/Glycine/SDS/Ethanol transfer buffer [0.001 M Tris-HCl; 0.2 M Glycine;
696 0.1% (w/v) SDS; 20% (v/v) ethanol]. The PVDF membrane was then blocked with a solution
697 of TBS (50 mM Tris-HCl pH 7.6; 150 mM NaCl) and 0.1% (v/v) Tween-20 with 5% (w/v)
698 skim milk powder. The primary antibody diluted in TBS-0.1% (v/v) Tween-20 solution with
699 5% (m/v) of skim milk powder was incubated with the membrane at 4°C for 12 hours. After 3
700 washes of 15 minutes with gentle agitation in TBS-0.1% (v/v) Tween-20 solution, the
701 membrane was incubated with HRP-conjugated secondary antibody (horseradish peroxidase –
702 goat anti-mouse or rabbit J. Immunoresearch SA, 1:10000) in the same solution at room
703 temperature for 1 hour. After 3 more washes of 15 minutes as previously described, the proteins
704 of interest were detected using Immobilon reagent (Millipore) and visualized with a LAS600
705 imager (Amersham).
706
707 **qRT-PCR**
708 Total RNA was prepared from neurons or tissue using 700 µL of TRIZOL reagent (Invitrogen)
709 according to the manufacturer's instructions. The RNA was then precipitated for 12 hours with
710 two volumes of 100% isopropanol at -20°C. After centrifugation for 10 minutes at 13,000 rpm
711 at 4°C, the supernatant was removed, and the RNA pellet was washed three times with 70%
712 ethanol (v/v). The pellet was then resuspended in 10 µL of mQ water, and the RNA
713 concentration was measured using a Nanodrop device. A DNase Turbo (ThermoFisher, 65001)

714 treatment was performed on 4 µg of RNA for 30 minutes at 37°C with 1 U of the enzyme to
715 eliminate any contamination by genomic DNA.
716 Reverse transcription was performed with SuperScript IV reverse transcriptase (Invitrogen)
717 using 500 ng of purified total RNA according to the manufacturer's instructions. qPCR was
718 performed with the LightCycler 480 SYBR Green I Master (Roche) according to the
719 manufacturer's instructions using the Roche LightCycler 480 device with an activation cycle of
720 15 minutes at 95°C and 45 amplification cycles (15 seconds at 95°C, 30 seconds at 60°C, 30
721 seconds at 70°C).
722
723 **Immunofluorescence**
724 Cells on coverslips were washed twice with 1x PBS to remove any residual media or debris.
725 Subsequently, they were fixed with 4% (v/v) formaldehyde and 4% (m/v) sucrose in 1x PBS
726 for 20 minutes. After fixation, the samples were washed twice again with 1x PBS.
727 Permeabilization was carried out using 0.2% (v/v) Triton X-100 in 1x PBS for 10 minutes. For
728 the blocking of unspecific sites, samples were incubated in a blocking buffer containing 1x
729 PBS, 3% (m/v) bovine serum albumin (BSA), and 0.02% (v/v) Triton X-100 for 1 hour. Primary
730 antibody incubation was performed overnight at 4°C. The primary antibody was diluted in a
731 buffer containing 0.02% (v/v) Triton X-100 and 0.2% BSA (m/v). The next day, samples were
732 washed three times for 10 minutes each with PBS containing 0.02% (v/v) Triton X-100 and
733 0.2% (m/v) BSA. Coverslips were then incubated for 1-2 hours at room temperature with
734 fluorophore-conjugated secondary antibodies, diluted 1:1000 in the same buffer used for the
735 primary antibody. After the secondary antibody incubation, samples were washed again three
736 times for 10 minutes each with PBS containing 0.02% (v/v) Triton X-100 and 0.2% (m/v) BSA.
737 Finally, the samples were mounted with Fluoromount and sealed with nail polish to prevent
738 drying and preserve fluorescence.
739
740 **Dendritic spine morphology classification**
741 Hippocampal primary neurons were magnetofected using NeuroMag (OzBiosciences) with a
742 GFP plasmid at 3DIV. At 21DIV, neurons were immunolabeled using a GFP-specific antibody
743 to enhance the signal. Selected isolated dendrites were imaged using confocal microscopy
744 (Leica SP8X) with a 63X objective and a resolution of 4096x4096 pixels, with a step size of
745 0.2 µm to generate a stack of images for subsequent automated analysis using Imaris software.
746 The following parameters were used to automatically classify dendritic spine according to their

747 morphology: stubby: spine length < 1 µm; mushroom: spine length < 3 µm and max head width
748 > mean neck width x 1.5; long thin: mean head width ≥ mean neck width and spine length >
749 1.5 µm; filopodia: spine length > 2 µm.
750
751 **MEA recording**
752 High-density MEA Accura (3Brain) chips having 4096 electrodes were sterilized by filling the
753 reservoir with 70% (v/v) ethanol for 20 minutes. Subsequently, the chips were rinsed three
754 times with sterile mQ water. Once dried, the central areas of the chip, which contain the
755 electrodes, were double-coated overnight with poly-D-lysine (P9155, Sigma) and bovine
756 fibronectin (F1141, Sigma). Following three additional washes with mQ water, exactly 80,000
757 dissociated primary neuronal progenitors were seeded onto the dry chips. After allowing one
758 hour for cell attachment, the reservoir was filled with Neurobasal Medium supplemented with
759 B27. Throughout the experiment, the chips were maintained at 37°C with 5% CO2 in a 10 cm
760 Petri dish with a smaller dish containing water to prevent media evaporation. Neurons were fed
761 every two days by replacing half of the media with pre-heated media. At 21DIV, the HD-MEA
762 chips were connected to the Biocam X device for recording neuronal activity using BrainWave
763 5 software. For DHPG treatment, a solution of 200 µM DHPG diluted in Neurobasal Medium
764 supplemented with B27 was prepared and pre-heated at 37°C. For neuronal activation, while
765 recording, half of the media in the HD-MEA chip was replaced with the DHPG-containing
766 Neurobasal Medium supplemented with B27 to achieve a final concentration of 100 µM DHPG.
767
768 **CLIP**
769 CLIP analysis was performed as described in (Tabet et al. 2016). Briefly, neuronal cultures at
770 8DIV were rinsed once with cold 1x PBS, and then proceeded for UV crosslinking (254 nm,
771 400 J/cm^2, Stratalinker) on ice. Neurons from 2 wells of 6-well plate equivalent to one embryo
772 were lysed in 400 µL of lysis buffer [50 mM Tris·HCl, pH 7.4, 100 mM KCl, 1 mM MgCl2,
773 0.1 mM CaCl2, 0.1% SDS, 1% Nonidet P-40, 0.5% sodium deoxycholate, 30 U of RNasin
774 (Promega), and 10 U of DNase Turbo (Invitrogen)] and incubated for 5 min at 37 °C. Lysates
775 were spun down at 18,000 g at 4 °C, and supernatants were precleared by incubation with 25
776 µL of free Dynabeads protein G (ThermoFisher) and then on 25 µL of Dynabeads protein G
777 coupled to rabbit anti-mouse IgGs (2.5 µg) for 1 h each. The lysates were then incubated
778 overnight with agitation on 25 µL of Dynabeads protein G coupled to 2.5 µg of anti-FMRP
779 antibody (ab264380, Abcam). Importantly, although RNase treatment of immunoprecipitated

780 RNA was not performed, partial RNA digestion occurs during the overnight incubation. After
781 immunoprecipitation, the supernatants were saved for RNA extraction (WT and *Fmr1*-KO
782 "inputs"), and the beads were washed three times with 400 µL of high-salt washing buffer [50
783 mM Tris·HCl, pH 7.4, 1 M KCl, 1 mM EDTA, 1% (v/v) Nonidet P-40, 0.5% (m/v) sodium
784 deoxycholate, and 0.1% (v/v) SDS, 4 °C]. RNAs from WT and *Fmr1*-KO neurons were
785 recovered by treatment of the beads with 0.4 mg of proteinase K in buffer (100 mM Tris·HCl,
786 pH 7.4, 50 mM NaCl, and 10 mM EDTA) for 20 min at 37 °C. The anti-FMRP antibody was
787 selected among several tested antibodies based on its ability to immunoprecipitated efficiently
788 some mRNAs considered as validated FMRP targets (i.e., *Dlg4, Map1b*) compared with
789 mRNAs considered as non-FMRP targets (*Rplp0*) in WT compared with *Fmr1*-KO neuron
790 extracts as quantified by qRT-PCR.
791 For the modified iCLIP method (individual-nucleotide resolution UV crosslinking and
792 immunoprecipitation) [99], the RNA crosslinked to FMRP was digested with proteinase K,
793 generating small polypeptides cross-linked to RNA that can induce reverse transcription arrests
794 (RT-stops) during cDNA synthesis, thereby allowing mapping of crosslink site. Detection of
795 RT-stop events across the *Dgkκ* transcript was performed with 18 *Dgkκ*-specific primers spaced
796 approximately 100 nucleotides apart, ensuring uniform reverse transcription coverage. RNA
797 extracted from WT and *Fmr1*-KO immunoprecipitated samples, as well as input brain total
798 RNA, underwent reverse transcription under identical conditions.
799
800 **RNA isolation and sequencing**
801 RNA was extracted from WT or *Fmr1*-KO neuron inputs (Input WT) or from CLIP samples
802 (CLIP WT and CLIP *Fmr1*-KO) using phenol/chloroform (vol/vol) followed by
803 chloroform/isoamyl alcohol (24:1) extraction and ethanol precipitation in the presence of 0.3
804 M sodium acetate. Subsequently, total RNA was treated with DNase (Invitrogen, AM1907) and
805 500 ng of RNA was ribodepleted using the Mouse-Rat RiboPOOL kit (siTOOLs Biotech,
806 catalog no. dp-K012-055) according to the manufacturer's protocol, followed by reverse
807 transcription using SuperScript IV (ThermoFisher, 18090200). For the HITS-CLIP strategy in
808 hypothalamic neurons, reverse transcription was conducted with random hexamers following
809 the manufacturer's protocol (ThermoFisher, N8080127). For the iCLIP strategy in cortical
810 neurons, a set of 18 *Dgkκ*-specific primers was utilized to cover the entire transcript of *Dgkκ*
811 and optimize RNA-seq coverage.

812 To enhance primer hybridization to *Dgkκ* mRNA, we modified the reverse transcription
813 protocol: after 5 minutes of RNA denaturation at 65°C, a hot start at 55°C was initiated by
814 adding the reverse transcriptase mix directly to the RNA. Unlike random hexamers, which can
815 initiate reverse transcription at multiple sites, this method allows reverse transcriptase to start
816 only at the specific positions defined by the primers. This approach helps in blocking
817 reinitiation when encountering FMRP polypeptide generated by proteinase K digestion,
818 resulting in an enrichment of transcript stop at the same 5' location. Generated cDNA was
819 treated with 1 µL of RNase A (5 µg/mL) for 20 minutes at 37°C, then purified using RNA XP
820 beads (Beckman Coulter) at a 1.8x ratio. The purified cDNA was sonicated in Covaris
821 microtubes (AFA fiber Snap-cap). Finally, the fragmented cDNA was repurified with RNA XP
822 beads and processed for MeDIP library preparation.
823
824 **EMSA**
825 The FMRP full-length protein (Isoform 1) was prepared as a fusion protein with GST in a
826 baculovirus system according to Bardoni et al. (1999). His–FMRP was eluted from NiNTA
827 beads (Qiagen) in elution buffer (50 mM Tris–HCl pH 7.5, 1 mM MgCl2, 150 mM KCl, 1 mM
828 EDTA, 1 mM DTT, 0.5M urea, 500 mM Imidazole). For binding assays, RNAs
829 (5'GCCGGCCCCAGAGCCGG(m^6A)CCCCGA(m^6A)CCAG(m^6A)CUCAGAGCCGGCCCC
830 AGAGCCGG(m^6A)CCCCGA(m^6A)CCAG(m^6A)CUCAGA(m^6A)CCG-Biotin 3') 5′-end
831 labeling of RNA was performed with T4 polynucleotide kinase and [γ-32P] ATP. Labeled
832 RNAs were purified on an 8% polyacrylamide gel (Acryl/Bisacrylamide 19/1, EU0061-B,
833 Euromodex) in 8 M urea. Labeled RNAs (40,000 c.p.m.), renatured for 10 min at 40°C in
834 binding buffer [10 mM HEPES, pH 7.4, 50 mM KCl, 1 mM DDT, 1 mM EDTA, 0.05%
835 TritonX-100, 5% (v/v) glycerol, 1 µg/µl yeast tRNA, and 2 U/µl ribonuclease inhibitor] were
836 incubated in 10 µl of binding buffer with 0–0.5 pmol at 25 °C for 30 min. The mixture was
837 loaded on a 4% polyacrylamide gel (bisacrylamide:acrylamide 1:37.5, 2.5% (v/v) glycerol, 0.5×
838 TBE) and migration was performed for 1h at 300 V at 4°C. The gel was then subjected to
839 phosphoimaging.
840
841 **RNA- nHU**
842 Protein-nHU analysis adapted from [43], was applied to RNA as follows: 8 days *in vitro* (8DIV)
843 cortical neurons cultures from three embryos were washed once with cold 1x PBS, pelleted at
844 1000g for 5 min at 4°C, and snap-frozen in liquid nitrogen. The pellets were lysed in ice-cold

845 lysis buffer [50 mM Hepes-KOH pH 7.5, 100 mM NaCl, 50 mM KCl, 4 mM MgCl2, 1% (v/v)
846 TritonX, 0.5 mM DTT, 1× cOmplete EDTA-free protease inhibitor cocktail, 5 mM TCEP, 10%
847 (v/v) glycerol, and 500 U/mL of RNasin]. Lysates underwent four rounds of sonication (4 × 20
848 s with 1-s pulses) on ice and were then incubated rotating at 4°C for 30 min. After centrifugation
849 at 12,000 rpm at 4°C for 20 min, the supernatant was collected for further analysis. The total
850 protein concentration was determined using the Bradford method (Bio-Rad protein assay dye
851 reagent, no. 5000006) with a BSA calibration curve (MP Biomedicals, no. 160069), measured
852 on a Bio-Rad SmartSpec 3000 spectrophotometer. Lysates were diluted to a concentration of 1
853 mg/ml.
854 For saturating streptavidin resin with biotinylated RNA probes or biotin, 50 µl of streptavidin
855 resin was mixed with biotin or RNA probes at 20 µM concentration in 6 to 6.5 volumes of resin
856 for 60 min. Specifically, the streptavidin resin (Streptavidin Sepharose High Performance,
857 Cytiva) was saturated with biotinylated EPAP RNA probes, with or without m^6A modifications,
858 at a concentration of 20 µM in 20 volumes of resin for 60 min. After saturation, the resins were
859 washed once with 10 volumes of holdup buffer (50 mM Tris-HCL pH 7.5, 300 mM NaCl, 1
860 mM TCEP, 40 U/mL RNasin, 0.22-µm filtered), and any remaining streptavidin beads were
861 blocked with 100 µM biotin in 10 volumes of holdup buffer for 10 min. Finally, the resins were
862 washed twice with 10 volumes of holdup buffer. The nHU mixture was then incubated at 4°C
863 for 1 hour. After incubation, the resin was separated from the supernatant by brief centrifugation
864 (15 sec, 2000 g), and half of the supernatant was immediately pipetted off to prevent resin
865 contamination.
866
867 **RNA pull-down**
868 For beads coupling, 45 µL of Dynabeads MyOne Streptavidin (ThermoFischer, 65001) were
869 incubated with RNA binding buffer [50 mM HEPES, pH 7.5, 150 mM NaCl, 0.5% (v/v) NP40,
870 10 mM MgCl2] containing 0.8 U/µL RNasin (Promega) for 30 minutes on ice. After removing
871 the supernatant to eliminate RNAse-RNasin complexes, the beads were blocked in RNA
872 binding buffer supplemented with 50 µg/mL yeast tRNA for 1 hour at 4°C under head-over-tail
873 agitation. Following two washes with RNA binding buffer, 5 µg of RNA probes were added to
874 the beads in 600 µL of RNA binding buffer and incubated for 1 hour at 4°C under head-over-
875 tail agitation. Subsequently, RNA-bead complexes were washed twice with RNA binding
876 buffer and twice with lysis buffer [50 mM Tris-HCl, pH 7.5, 150 mM KCl, 1 mM MgCl2, 1

877 mM EDTA, 1% (v/v) NP40, 0.5 mM DTT, 1× complete EDTA-free protease inhibitor cocktail,
878 2.5% (v/v) glycerol, RNasin 200 U/mL].
879 Pellets of cortical neurons, equivalent to 5 embryos, were lysed in 300 µL of lysis buffer and
880 incubated for 15 minutes at 4°C under head-over-tail agitation. After centrifugation at 1000 x
881 g for 10 minutes at 4°C, the pellets corresponding to the nuclei fraction were resuspended in
882 300 µL of lysis buffer, sonicated (5 x 30 seconds pulses), and combined with the cytosol
883 fraction. Lysates were then centrifuged at 18,000 x g for 10 minutes at 4°C, and protein
884 concentration was determined using the Bradford method. Subsequently, 500 µg of protein
885 lysate was incubated with RNA-bead complexes in 600 µL of lysis buffer for 1 hour under
886 head-over-tail agitation. Finally, beads were washed three times with lysis buffer and stored
887 dried at -20°C until proteomic analysis.
888
889 **Northern-blot**
890 Cell pellets were lysed on ice in 300 µL lysis buffer consisting of 50 mM Tris-HCl pH 7.5, 5
891 mM MgCl2, 150 mM KCl, 1 mM DTT, 0.5% NP-40, cycloheximide (100 µg/mL final), and
892 protease inhibitor cocktail. After gentle pipetting, lysate was centrifuged at 7000 x g for 8 min
893 and RNA concentration was quantified using the Qubit BR RNA assay (Thermo Fisher).
894 An aliquot corresponding to 25 µg total RNA was adjusted to 300 µL using lysis buffer, and
895 RNase A digestion was initiated by addition of 0.8 µg RNase A (Thermo Fisher, R1253).
896 Samples were incubated at 25 °C for 20 min. Digestions were stopped by addition of TRIzol
897 (Invitrogen) and RNA was extracted according to the manufacturer's instructions. Ten
898 micrograms of purified RNA were loaded per lane for subsequent Northern blot analysis. After
899 migration, gel was stained with ethidium bromide for imaging and RNA was electrotransfered
900 onto a positively charged nylon membrane (Cytivia, 25006218) and proceeded twice to UV
901 crosslinking (254 nm, 1200 J, Stratalinker).
902
903 PCR product (~ 400 nt) spanning the region of interest were radioactively labeled using random
904 priming. Briefly, 100 ng of purified DNA probe were mixed with 2 µL of random hexamers
905 (Thermo Fisher, N8080127) in a final volume of 15 µL, heated to 95 °C for 5 min, and rapidly
906 chilled on ice for ≥2 min. The denatured probes were then combined with 6 µL of cold dNTP
907 mix (0.5 mM each of dATP, dGTP, and dTTP), 5 µL of 10x Klenow buffer, 5 µL of [α-32P]-
908 dCTP, 1 µL of Klenow fragment (Thermo Fisher), and nuclease-free water to a final reaction

909 volume of 50 µL. The labeling reaction was incubated at 37 °C for 2 h. Probes were then
910 purified using MicroSpin G-50 columns (Cytivia, 27533001).
911 Following labeling, probes were diluted by adding 760 µL of nuclease-free water. For
912 hybridization, 400 µL of probe (~50 ng DNA) were heated to 95 °C for 5 min to denature, then
913 immediately added to ~5 mL of hybridization solution (6x SSC [150 mM NaCl, 15 mM sodium
914 citrate], 0.5% SDS). Membranes were incubated with the denatured probe overnight at 60 °C.
915 Membranes were washed twice with SSC 2x, and once with SSC 2x, 0.1 % SDS for 10 min at
916 60°C. Finally, the membranes were then subjected to phosphoimaging.
917
918 **Peak calling, filtration and annotation**
919 The analyses of the CLIP-Seq dataset were implemented on Galaxy [100]. The protocol was
920 adapted from [101]. In brief, adapters were removed and reads from fastq files of CLIP-Seq (IP)
921 and bulk RNA-Seq (Input) were trimmed using Trimmomatic [102] (Galaxy Version
922 0.39+galaxy2). Reads were then aligned on the Mouse reference genome mm39 using STAR
923 [103] (Galaxy Version 2.7.11b+galaxy0). Duplicates were removed with Sambamba [104] (Galaxy
924 Version 1.0.1+galaxy2). Peaks were called using PEAKachu
925 (https://github.com/tbischler/PEAKachu) (Galaxy Version 0.2.0+galaxy0), with the bam of
926 bulk RNA-Seq data as control. Simultaneously, we estimated gene expression by counting reads
927 aligned on each gene as define in the reference annotation Gencode v. M38 with FeatureCounts
928 [105] (Galaxy Version 2.1.1+galaxy0). Only genes with a count of at least 50 reads in either CLIP-
929 Seq data or RNA-Seq data were further analyzed. We performed a differential expression
930 analysis between RNA-Seq and CLIP-seq transcriptomic profiles with limma (limma-voom)
931 [106] (Galaxy Version 3.58.1+galaxy0).
932 The peaks detected with PEAKachu (https://github.com/tbischler/PEAKachu) were further
933 filtered and annotated. We first removed peaks for which expression in the RNA-Seq was null
934 (noted Inf by PEAKachu). For annotation, we used the BioMart tool [107] to extract coordinates,
935 strand for canonical transcripts of the mouse genome annotation. We then only kept peaks
936 overlapping annotated exons on the same strand with IntersectBed for the Bedtools suite [108].
937 We further kept peaks overlapping genes found over-expressed in the CLIP-Seq dataset when
938 compared to the RNA-Seq dataset (with limma).
939 To convert the RNA sequence under the peaks, we used the R package geno2proteo [109]. We
940 then counted the frequency each amino acid under the remaining peaks (**Supplementary Table**
941 **S2**).

942 **Data availability**

943

944 Clip-seq data are available in GEO repository under accession number GSE324369.

945

946 **References**

947 1. Hagerman, R.J., Berry-Kravis, E., Hazlett, H.C., Bailey, D.B., Jr., Moine, H., Kooy, R.F.,
948 Tassone, F., Gantois, I., Sonenberg, N., Mandel, J.L., et al. (2017). Fragile X syndrome.
949 Nat Rev Dis Primers *3*, 17065. https://doi.org/10.1038/nrdp.2017.65.

950 2. Napoli, I., Mercaldo, V., Boyl, P.P., Eleuteri, B., Zalfa, F., De Rubeis, S., Di Marino, D.,
951 Mohr, E., Massimi, M., Falconi, M., et al. (2008). The fragile X syndrome protein
952 represses activity-dependent translation through CYFIP1, a new 4E-BP. Cell *134*, 1042–
953 1054. https://doi.org/10.1016/j.cell.2008.07.031.

954 3. Brown, M.R., Kronengold, J., Gazula, V.R., Chen, Y., Strumbos, J.G., Sigworth, F.J.,
955 Navaratnam, D., and Kaczmarek, L.K. (2010). Fragile X mental retardation protein
956 controls gating of the sodium-activated potassium channel Slack. Nat Neurosci *13*, 819–
957 821. https://doi.org/10.1038/nn.2563.

958 4. Bhogal, B., Jepson, J.E., Savva, Y.A., Pepper, A.S.-R., Reenan, R.A., and Jongens, T.A.
959 (2011). Modulation of dADAR-dependent RNA editing by the Drosophila fragile X
960 mental retardation protein. Nat Neurosci *14*, 1517–1524. https://doi.org/10.1038/nn.2950.

961 5. Darnell, J.C., Van Driesche, S.J., Zhang, C., Hung, K.Y., Mele, A., Fraser, C.E., Stone,
962 E.F., Chen, C., Fak, J.J., Chi, S.W., et al. (2011). FMRP stalls ribosomal translocation on
963 mRNAs linked to synaptic function and autism. Cell *146*, 247–261.
964 https://doi.org/10.1016/j.cell.2011.06.013.

965 6. Alpatov, R., Lesch, B.J., Nakamoto-Kinoshita, M., Blanco, A., Chen, S., Stutzer, A.,
966 Armache, K.J., Simon, M.D., Xu, C., Ali, M., et al. (2014). A chromatin-dependent role
967 of the fragile X mental retardation protein FMRP in the DNA damage response. Cell *157*,
968 869–881. https://doi.org/10.1016/j.cell.2014.03.040.

969 7. Richter, J.D., Bassell, G.J., and Klann, E. (2015). Dysregulation and restoration of
970 translational homeostasis in fragile X syndrome. Nat Rev Neurosci *16*, 595–605.
971 https://doi.org/10.1038/nrn4001.

972 8. Shamay-Ramot, A., Khermesh, K., Porath, H.T., Barak, M., Pinto, Y., Wachtel, C.,
973 Zilberberg, A., Lerer-Goldshtein, T., Efroni, S., Levanon, E.Y., et al. (2015). Fmrp
974 Interacts with Adar and Regulates RNA Editing, Synaptic Density and Locomotor
975 Activity in Zebrafish. PLoS Genet *11*, e1005702.
976 https://doi.org/10.1371/journal.pgen.1005702.

977 9. Zhang, F., Kang, Y., Wang, M., Li, Y., Xu, T., Yang, W., Song, H., Wu, H., Shu, Q., and
978 Jin, P. (2018). Fragile X mental retardation protein modulates the stability of its m6A-
979 marked messenger RNA targets. Hum Mol Genet *27*, 3936–3950.
980 https://doi.org/10.1093/hmg/ddy292.

10. Kurosaki, T., Cho, H., Abshire, E.T., Pröschel, C., Mitsutomi, S., Sato, H., Simko, E.A.J., Fraser, C.S., Sakano, H., and Maquat, L.E. (2025). FMRP drives mRNP targets into translationally silenced complexes. Mol Cell *85*, 2956-2972.e10. https://doi.org/10.1016/j.molcel.2025.06.012.

11. Fmr1 knockout mice: a model to study fragile X mental retardation. The Dutch-Belgian Fragile X Consortium. (1994). Cell *78*, 23–33.

12. Bear, M.F., Huber, K.M., and Warren, S.T. (2004). The mGluR theory of fragile X mental retardation. Trends Neurosci *27*, 370–377.

13. Comery, T.A., Harris, J.B., Willems, P.J., Oostra, B.A., Irwin, S.A., Weiler, I.J., and Greenough, W.T. (1997). Abnormal dendritic spines in fragile X knockout mice: maturation and pruning deficits. Proc Natl Acad Sci U S A *94*, 5401–5404.

14. Nimchinsky, E.A., Oberlander, A.M., and Svoboda, K. (2001). Abnormal development of dendritic spines in FMR1 knock-out mice. J Neurosci *21*, 5139–5146.

15. Irwin, S.A., Idupulapati, M., Gilbert, M.E., Harris, J.B., Chakravarti, A.B., Rogers, E.J., Crisostomo, R.A., Larsen, B.P., Mehta, A., Alcantara, C.J., et al. (2002). Dendritic spine and dendritic field characteristics of layer V pyramidal neurons in the visual cortex of fragile-X knockout mice. Am J Med Genet *111*, 140–146. https://doi.org/10.1002/ajmg.10500.

16. McKinney, B.C., Grossman, A.W., Elisseou, N.M., and Greenough, W.T. (2005). Dendritic spine abnormalities in the occipital cortex of C57BL/6 Fmr1 knockout mice. Am J Med Genet B Neuropsychiatr Genet *136B*, 98–102. https://doi.org/10.1002/ajmg.b.30183.

17. Grossman, A.W., Aldridge, G.M., Weiler, I.J., and Greenough, W.T. (2006). Local protein synthesis and spine morphogenesis: Fragile X syndrome and beyond. J Neurosci *26*, 7151–7155.

18. Greenough, W.T., Klintsova, A.Y., Irwin, S.A., Galvez, R., Bates, K.E., and Weiler, I.J. (2001). Synaptic regulation of protein synthesis and the fragile X protein. Proc Natl Acad Sci U S A *98*, 7101–7106.

19. Qin, M., Kang, J., Burlin, T.V., Jiang, C., and Smith, C.B. (2005). Postadolescent changes in regional cerebral protein synthesis: an in vivo study in the FMR1 null mouse. J Neurosci *25*, 5087–5095. https://doi.org/10.1523/JNEUROSCI.0093-05.2005.

20. Dolen, G., Osterweil, E., Rao, B.S., Smith, G.B., Auerbach, B.D., Chattarji, S., and Bear, M.F. (2007). Correction of fragile X syndrome in mice. Neuron *56*, 955–962.

21. Osterweil, E.K., Krueger, D.D., Reinhold, K., and Bear, M.F. (2010). Hypersensitivity to mGluR5 and ERK1/2 leads to excessive protein synthesis in the hippocampus of a mouse model of fragile X syndrome. J Neurosci *30*, 15616–15627. https://doi.org/10.1523/JNEUROSCI.3888-10.2010.

22. Bechara, E.G., Didiot, M.C., Melko, M., Davidovic, L., Bensaid, M., Martin, P., Castets, M., Pognonec, P., Khandjian, E.W., Moine, H., et al. (2009). A novel function for fragile X mental retardation protein in translational activation. PLoS Biol *7*, e16.

1020 23. Tabet, R., Moutin, E., Becker, J.A., Heintz, D., Fouillen, L., Flatter, E., Krezel, W., Alunni,
1021 V., Koebel, P., Dembele, D., et al. (2016). Fragile X Mental Retardation Protein (FMRP)
1022 controls diacylglycerol kinase activity in neurons. Proc Natl Acad Sci U S A *113*, E3619-
1023 28. https://doi.org/10.1073/pnas.1522631113.

1024 24. Ascano, M., Jr., Mukherjee, N., Bandaru, P., Miller, J.B., Nusbaum, J.D., Corcoran, D.L.,
1025 Langlois, C., Munschauer, M., Dewell, S., Hafner, M., et al. (2012). FMRP targets distinct
1026 mRNA sequence elements to regulate protein expression. Nature *492*, 382–386.
1027 https://doi.org/10.1038/nature11737.

1028 25. Maurin, T., Lebrigand, K., Castagnola, S., Paquet, A., Jarjat, M., Popa, A., Grossi, M.,
1029 Rage, F., and Bardoni, B. (2018). HITS-CLIP in various brain areas reveals new targets
1030 and new modalities of RNA binding by fragile X mental retardation protein. Nucleic Acids
1031 Res *46*, 6344–6355. https://doi.org/10.1093/nar/gky267.

1032 26. Darnell, J.C., Jensen, K.B., Jin, P., Brown, V., Warren, S.T., and Darnell, R.B. (2001).
1033 Fragile X mental retardation protein targets G quartet mRNAs important for neuronal
1034 function. Cell *107*, 489–499.

1035 27. Schaeffer, C., Bardoni, B., Mandel, J.L., Ehresmann, B., Ehresmann, C., and Moine, H.
1036 (2001). The fragile X mental retardation protein binds specifically to its mRNA via a
1037 purine quartet motif. Embo J *20*, 4803–4813.

1038 28. Habbas, K., Cakil, O., Zámbó, B., Tabet, R., Riet, F., Dembele, D., Mandel, J.-L.,
1039 Hocquemiller, M., Laufer, R., Piguet, F., et al. (2022). AAV-delivered diacylglycerol
1040 kinase DGKk achieves long-term rescue of fragile X syndrome mouse model. EMBO Mol
1041 Med *14*, e14649. https://doi.org/10.15252/emmm.202114649.

1042 29. Li, Z., Zhang, Y., Ku, L., Wilkinson, K.D., Warren, S.T., and Feng, Y. (2001). The fragile
1043 X mental retardation protein inhibits translation via interacting with mRNA. Nucleic
1044 Acids Res *29*, 2276–2283.

1045 30. Tabet, R., Vitale, N., and Moine, H. (2016). Fragile X syndrome: Are signaling lipids the
1046 missing culprits? Biochimie. https://doi.org/10.1016/j.biochi.2016.09.002.

1047 31. Moine, H., and Vitale, N. (2019). Of local translation control and lipid signaling in neurons.
1048 Adv Biol Regul *71*, 194–205. https://doi.org/10.1016/j.jbior.2018.09.005.

1049 32. Edens, B.M., Vissers, C., Su, J., Arumugam, S., Xu, Z., Shi, H., Miller, N., Rojas Ringeling,
1050 F., Ming, G.-L., He, C., et al. (2019). FMRP Modulates Neural Differentiation through
1051 m(6)A-Dependent mRNA Nuclear Export. Cell Rep *28*, 845-854.e5.
1052 https://doi.org/10.1016/j.celrep.2019.06.072.

1053 33. Worpenberg, L., Paolantoni, C., Longhi, S., Mulorz, M.M., Lence, T., Wessels, H.-H.,
1054 Dassi, E., Aiello, G., Sutandy, F.X.R., Scheibe, M., et al. (2021). Ythdf is a N6-
1055 methyladenosine reader that modulates Fmr1 target mRNA selection and restricts axonal
1056 growth in Drosophila. EMBO J *40*, e104975. https://doi.org/10.15252/embj.2020104975.

1057 34. Shafik, A.M., Zhang, F., Guo, Z., Dai, Q., Pajdzik, K., Li, Y., Kang, Y., Yao, B., Wu, H.,
1058 He, C., et al. (2021). N6-methyladenosine dynamics in neurodevelopment and aging, and

1059 its potential role in Alzheimer's disease. Genome Biol *22*, 17.
1060 https://doi.org/10.1186/s13059-020-02249-z.

1061 35. Murakami, S., and Jaffrey, S.R. (2022). Hidden codes in mRNA: Control of gene
1062 expression by m(6)A. Mol Cell *82*, 2236–2251.
1063 https://doi.org/10.1016/j.molcel.2022.05.029.

1064 36. Liu, J., Yue, Y., Han, D., Wang, X., Fu, Y., Zhang, L., Jia, G., Yu, M., Lu, Z., Deng, X., et
1065 al. (2014). A METTL3-METTL14 complex mediates mammalian nuclear RNA N6-
1066 adenosine methylation. Nat Chem Biol *10*, 93–95.
1067 https://doi.org/10.1038/nchembio.1432.

1068 37. Lee, Y., Choe, J., Park, O.H., and Kim, Y.K. (2020). Molecular Mechanisms Driving
1069 mRNA Degradation by m(6)A Modification. Trends Genet *36*, 177–188.
1070 https://doi.org/10.1016/j.tig.2019.12.007.

1071 38. Arguello, A.E., DeLiberto, A.N., and Kleiner, R.E. (2017). RNA Chemical Proteomics
1072 Reveals the N(6)-Methyladenosine (m(6)A)-Regulated Protein-RNA Interactome. J Am
1073 Chem Soc *139*, 17249–17252. https://doi.org/10.1021/jacs.7b09213.

1074 39. Edupuganti, R.R., Geiger, S., Lindeboom, R.G.H., Shi, H., Hsu, P.J., Lu, Z., Wang, S.-Y.,
1075 Baltissen, M.P.A., Jansen, P.W.T.C., Rossa, M., et al. (2017). N(6)-methyladenosine
1076 (m(6)A) recruits and repels proteins to regulate mRNA homeostasis. Nat Struct Mol Biol
1077 *24*, 870–878. https://doi.org/10.1038/nsmb.3462.

1078 40. Kan, L., Ott, S., Joseph, B., Park, E.S., Dai, W., Kleiner, R.E., Claridge-Chang, A., and Lai,
1079 E.C. (2021). A neural m(6)A/Ythdf pathway is required for learning and memory in
1080 Drosophila. Nat Commun *12*, 1458. https://doi.org/10.1038/s41467-021-21537-1.

1081 41. Zhang, G., Xu, Y., Wang, X., Zhu, Y., Wang, L., Zhang, W., Wang, Y., Gao, Y., Wu, X.,
1082 Cheng, Y., et al. (2022). Dynamic FMR1 granule phase switch instructed by m6A
1083 modification contributes to maternal RNA decay. Nat Commun *13*, 859.
1084 https://doi.org/10.1038/s41467-022-28547-7.

1085 42. Flamand, M.N., and Meyer, K.D. (2022). m6A and YTHDF proteins contribute to the
1086 localization of select neuronal mRNAs. Nucleic Acids Res *50*, 4464–4483.
1087 https://doi.org/10.1093/nar/gkac251.

1088 43. Zambo, B., Morlet, B., Negroni, L., Trave, G., and Gogl, G. (2022). Native holdup (nHU)
1089 to measure binding affinities from cell extracts. Sci Adv *8*, eade3828.
1090 https://doi.org/10.1126/sciadv.ade3828.

1091 44. Dictenberg, J.B., Swanger, S.A., Antar, L.N., Singer, R.H., and Bassell, G.J. (2008). A
1092 direct role for FMRP in activity-dependent dendritic mRNA transport links filopodial-
1093 spine morphogenesis to fragile X syndrome. Dev Cell *14*, 926–939.

1094 45. Kao, D.I., Aldridge, G.M., Weiler, I.J., and Greenough, W.T. (2010). Altered mRNA
1095 transport, docking, and protein translation in neurons lacking fragile X mental retardation
1096 protein. Proc Natl Acad Sci U S A *107*, 15601–15606.
1097 https://doi.org/10.1073/pnas.1010564107.

46. Gutierrez, E., Shin, B.-S., Woolstenhulme, C.J., Kim, J.-R., Saini, P., Buskirk, A.R., and Dever, T.E. (2013). eIF5A promotes translation of polyproline motifs. Mol Cell *51*, 35–45. https://doi.org/10.1016/j.molcel.2013.04.021.

47. Zhao, T., Chen, Y.-M., Li, Y., Wang, J., Chen, S., Gao, N., and Qian, W. (2021). Disome-seq reveals widespread ribosome collisions that promote cotranslational protein folding. Genome Biol *22*, 16. https://doi.org/10.1186/s13059-020-02256-0.

48. Ito, Y., Chadani, Y., Niwa, T., Yamakawa, A., Machida, K., Imataka, H., and Taguchi, H. (2022). Nascent peptide-induced translation discontinuation in eukaryotes impacts biased amino acid usage in proteomes. Nat Commun *13*, 7451. https://doi.org/10.1038/s41467-022-35156-x.

49. Aguilar Rangel, M., Stein, K., and Frydman, J. (2024). A machine learning approach uncovers principles and determinants of eukaryotic ribosome pausing. Sci Adv *10*, eado0738. https://doi.org/10.1126/sciadv.ado0738.

50. Veltri, A.J., D'Orazio, K.N., Lessen, L.N., Loll-Krippleber, R., Brown, G.W., and Green, R. (2022). Distinct elongation stalls during translation are linked with distinct pathways for mRNA degradation. eLife *11*, e76038. https://doi.org/10.7554/eLife.76038.

51. Wu, C.C.-C., Peterson, A., Zinshteyn, B., Regot, S., and Green, R. (2020). Ribosome Collisions Trigger General Stress Responses to Regulate Cell Fate. Cell *182*, 404-416.e14. https://doi.org/10.1016/j.cell.2020.06.006.

52. Mao, Y., Dong, L., Liu, X.-M., Guo, J., Ma, H., Shen, B., and Qian, S.-B. (2019). m(6)A in mRNA coding regions promotes translation via the RNA helicase-containing YTHDC2. Nat Commun *10*, 5332. https://doi.org/10.1038/s41467-019-13317-9.

53. Linder, B., Sharma, P., Wu, J., Birbaumer, T., Eggers, C., Murakami, S., Ott, R.E., Fenzl, K., Vorgerd, H., Erhard, F., et al. (2025). tRNA modifications tune m(6)A-dependent mRNA decay. Cell *188*, 3715-3727.e13. https://doi.org/10.1016/j.cell.2025.04.013.

54. Murakami, S., Olarerin-George, A.O., Liu, J.F., Zaccara, S., Hawley, B., and Jaffrey, S.R. (2025). m(6)A alters ribosome dynamics to initiate mRNA degradation. Cell *188*, 3728-3743.e20. https://doi.org/10.1016/j.cell.2025.04.020.

55. Zhou, Y., Ćorović, M., Hoch-Kraft, P., Meiser, N., Mesitov, M., Körtel, N., Back, H., Naarmann-de Vries, I.S., Katti, K., Obrdlík, A., et al. (2024). m6A sites in the coding region trigger translation-dependent mRNA decay. Mol Cell *84*, 4576-4593.e12. https://doi.org/10.1016/j.molcel.2024.10.033.

56. Choi, J., Ieong, K.-W., Demirci, H., Chen, J., Petrov, A., Prabhakar, A., O'Leary, S.E., Dominissini, D., Rechavi, G., Soltis, S.M., et al. (2016). N(6)-methyladenosine in mRNA disrupts tRNA selection and translation-elongation dynamics. Nat Struct Mol Biol *23*, 110–115. https://doi.org/10.1038/nsmb.3148.

57. Jain, S., Koziej, L., Poulis, P., Kaczmarczyk, I., Gaik, M., Rawski, M., Ranjan, N., Glatt, S., and Rodnina, M.V. (2023). Modulation of translational decoding by m(6)A modification of mRNA. Nat Commun *14*, 4784. https://doi.org/10.1038/s41467-023-40422-7.

1138 58. Siomi, M.C., Zhang, Y., Siomi, H., and Dreyfuss, G. (1996). Specific sequences in the
1139 fragile X syndrome protein FMR1 and the FXR proteins mediate their binding to 60S
1140 ribosomal subunits and the interactions among them. Mol Cell Biol *16*, 3825–3832.

1141 59. George, J., Li, Y., Kadamberi, I.P., Parashar, D., Tsaih, S.-W., Gupta, P., Geethadevi, A.,
1142 Chen, C., Ghosh, C., Sun, Y., et al. (2021). RNA-binding protein FXR1 drives cMYC
1143 translation by recruiting eIF4F complex to the translation start site.
1144 https://doi.org/10.1016/j.celrep.2021.109934.

1145 60. van der Zanden, L.F., van Rooij, I.A., Feitz, W.F., Knight, J., Donders, A.R., Renkema,
1146 K.Y., Bongers, E.M., Vermeulen, S.H., Kiemeney, L.A., Veltman, J.A., et al. (2011).
1147 Common variants in DGKK are strongly associated with risk of hypospadias. Nat Genet
1148 *43*, 48–50. https://doi.org/10.1038/ng.721.

1149 61. Mientjes, E.J., Nieuwenhuizen, I., Kirkpatrick, L., Zu, T., Hoogeveen-Westerveld, M.,
1150 Severijnen, L., Rife, M., Willemsen, R., Nelson, D.L., and Oostra, B.A. (2006). The
1151 generation of a conditional Fmr1 knock out mouse model to study Fmrp function in vivo.
1152 Neurobiol Dis *21*, 549–555. https://doi.org/10.1016/j.nbd.2005.08.019.

1153 62. Leboucher, A., Bermudez-Martin, P., Mouska, X., Amri, E.-Z., Pisani, D.F., and
1154 Davidovic, L. (2019). Fmr1-Deficiency Impacts Body Composition, Skeleton, and Bone
1155 Microstructure in a Mouse Model of Fragile X Syndrome. Front Endocrinol (Lausanne)
1156 *10*, 678. https://doi.org/10.3389/fendo.2019.00678.

1157 63. Imai, S., Kai, M., Yasuda, S., Kanoh, H., and Sakane, F. (2005). Identification and
1158 characterization of a novel human type II diacylglycerol kinase, DGK kappa. J Biol Chem
1159 *280*, 39870–39881. https://doi.org/10.1074/jbc.M500669200.

1160 64. He, C.X., and Portera-Cailliau, C. (2013). The trouble with spines in fragile X syndrome:
1161 density, maturity and plasticity. Neuroscience *251*, 120–128.
1162 https://doi.org/10.1016/j.neuroscience.2012.03.049.

1163 65. Lee, D., Kim, E., and Tanaka-Yamamoto, K. (2016). Diacylglycerol Kinases in the
1164 Coordination of Synaptic Plasticity. Front Cell Dev Biol *4*, 92.
1165 https://doi.org/10.3389/fcell.2016.00092.

1166 66. Kong, J., and Lasko, P. (2012). Translational control in cellular and developmental
1167 processes. Nat Rev Genet *13*, 383–394. https://doi.org/10.1038/nrg3184.

1168 67. Biever, A., Valjent, E., and Puighermanal, E. (2015). Ribosomal Protein S6
1169 Phosphorylation in the Nervous System: From Regulation to Function. Front Mol
1170 Neurosci *8*, 75. https://doi.org/10.3389/fnmol.2015.00075.

1171 68. Chen, L., Yun, S.W., Seto, J., Liu, W., and Toth, M. (2003). The fragile X mental
1172 retardation protein binds and regulates a novel class of mRNAs containing U rich target
1173 sequences. Neuroscience *120*, 1005–1017.

1174 69. Dolzhanskaya, N., Sung, Y.J., Conti, J., Currie, J.R., and Denman, R.B. (2003). The fragile
1175 X mental retardation protein interacts with U-rich RNAs in a yeast three-hybrid system.
1176 Biochem Biophys Res Commun *305*, 434–441.

1177 70. Greenblatt, E.J., and Spradling, A.C. (2018). Fragile X mental retardation 1 gene enhances
1178 the translation of large autism-related proteins. Science *361*, 709–712.
1179 https://doi.org/10.1126/science.aas9963.

1180 71. Anadolu, M.N., Sun, J., Kailasam, S., Chalkiadaki, K., Krimbacher, K., Li, J.T.-Y.,
1181 Markova, T., Jafarnejad, S.M., Lefebvre, F., Ortega, J., et al. (2023). Ribosomes in RNA
1182 Granules Are Stalled on mRNA Sequences That Are Consensus Sites for FMRP
1183 Association. J Neurosci *43*, 2440–2459. https://doi.org/10.1523/JNEUROSCI.1002-
1184 22.2023.

1185 72. Li, J.T.-Y., Amiri, M., Kailasam, S., Sun, J., Sonenberg, N., Ortega, J., and Sossin, W.S.
1186 (2025). FMRP Regulates Neuronal RNA Granules Containing Stalled Ribosomes, Not
1187 Where Ribosomes Stall. https://doi.org/10.7554/elife.106692.1.

1188 73. Sundaramoorthy, E., Leonard, M., Mak, R., Liao, J., Fulzele, A., and Bennett, E.J. (2017).
1189 ZNF598 and RACK1 Regulate Mammalian Ribosome-Associated Quality Control
1190 Function by Mediating Regulatory 40S Ribosomal Ubiquitylation. Mol Cell *65*, 751-
1191 760.e4. https://doi.org/10.1016/j.molcel.2016.12.026.

1192 74. Juszkiewicz, S., Chandrasekaran, V., Lin, Z., Kraatz, S., Ramakrishnan, V., and Hegde,
1193 R.S. (2018). ZNF598 Is a Quality Control Sensor of Collided Ribosomes. Mol Cell *72*,
1194 469-481.e7. https://doi.org/10.1016/j.molcel.2018.08.037.

1195 75. Hashimoto, S., Sugiyama, T., Yamazaki, R., Nobuta, R., and Inada, T. (2020). Identification
1196 of a novel trigger complex that facilitates ribosome-associated quality control in
1197 mammalian cells. Sci Rep *10*, 3422. https://doi.org/10.1038/s41598-020-60241-w.

1198 76. Geng, J., Wang, X., Pan, J., Khan, D., Pimcharoen, S., Zhang, Y., Mosammaparast, N.,
1199 Hirose, S., Petrucelli, L., Brandman, O., et al. (2025). CRISPR activation of the ribosome-
1200 associated quality control factor ASCC3 ameliorates fragile X syndrome phenotypes in
1201 mice. Sci Transl Med *17*, eadq3551. https://doi.org/10.1126/scitranslmed.adq3551.

1202 77. Kazdoba, T.M., Leach, P.T., Silverman, J.L., and Crawley, J.N. (2014). Modeling fragile
1203 X syndrome in the Fmr1 knockout mouse. Intractable Rare Dis Res *3*, 118–133.
1204 https://doi.org/10.5582/irdr.2014.01024.

1205 78. Kim, K., Yang, J., Zhong, X.P., Kim, M.H., Kim, Y.S., Lee, H.W., Han, S., Choi, J., Han,
1206 K., Seo, J., et al. (2009). Synaptic removal of diacylglycerol by DGKzeta and PSD-95
1207 regulates dendritic spine maintenance. Embo J *28*, 1170–1179.
1208 https://doi.org/10.1038/emboj.2009.44.

1209 79. Shirai, Y., Kouzuki, T., Kakefuda, K., Moriguchi, S., Oyagi, A., Horie, K., Morita, S.Y.,
1210 Shimazawa, M., Fukunaga, K., Takeda, J., et al. (2010). Essential role of neuron-enriched
1211 diacylglycerol kinase (DGK), DGKbeta in neurite spine formation, contributing to
1212 cognitive function. PLoS One *5*, e11602. https://doi.org/10.1371/journal.pone.0011602.

1213 80. Yang, J., Seo, J., Nair, R., Han, S., Jang, S., Kim, K., Han, K., Paik, S.K., Choi, J., Lee, S.,
1214 et al. (2011). DGKiota regulates presynaptic release during mGluR-dependent LTD.
1215 Embo J *30*, 165–180. https://doi.org/10.1038/emboj.2010.286.

1216 81. Mérida, I., Avila-Flores, A., and Merino, E. (2008). Diacylglycerol kinases: at the hub of
1217 cell signalling. Biochem J *409*, 1–18. https://doi.org/10.1042/BJ20071040.

1218 82. Almena, M., and Merida, I. (2011). Shaping up the membrane: diacylglycerol coordinates
1219 spatial orientation of signaling. Trends Biochem Sci *36*, 593–603.
1220 https://doi.org/10.1016/j.tibs.2011.06.005.

1221 83. Eichmann, T.O., and Lass, A. (2015). DAG tales: the multiple faces of diacylglycerol--
1222 stereochemistry, metabolism, and signaling. Cell Mol Life Sci *72*, 3931–3952.
1223 https://doi.org/10.1007/s00018-015-1982-3.

1224 84. Cooke, M., and Kazanietz, M.G. (2022). Overarching roles of diacylglycerol signaling in
1225 cancer development and antitumor immunity. Sci Signal *15*, eabo0264.
1226 https://doi.org/10.1126/scisignal.abo0264.

1227 85. Leboucher, A., Pisani, D.F., Martinez-Gili, L., Chilloux, J., Bermudez-Martin, P., Van
1228 Dijck, A., Ganief, T., Macek, B., Becker, J.A.J., Le Merrer, J., et al. (2019). The
1229 translational regulator FMRP controls lipid and glucose metabolism in mice and humans.
1230 Mol Metab *21*, 22–35. https://doi.org/10.1016/j.molmet.2019.01.002.

1231 86. Ruggiero-Ruff, R.E., Villa, P.A., Hijleh, S.A., Avalos, B., DiPatrizio, N.V., Haga-
1232 Yamanaka, S., and Coss, D. (2023). Increased body weight in mice with fragile X
1233 messenger ribonucleoprotein 1 (Fmr1) gene mutation is associated with hypothalamic
1234 dysfunction. Sci Rep *13*, 12666. https://doi.org/10.1038/s41598-023-39643-z.

1235 87. Nowicki, S.T., Tassone, F., Ono, M.Y., Ferranti, J., Croquette, M.F., Goodlin-Jones, B.,
1236 and Hagerman, R.J. (2007). The Prader-Willi phenotype of fragile X syndrome. J Dev
1237 Behav Pediatr *28*, 133–138. https://doi.org/10.1097/01.DBP.0000267563.18952.c9.

1238 88. Hardiman, R.L., and Bratt, A. (2016). Hypothalamic-pituitary-adrenal axis function in
1239 Fragile X Syndrome and its relationship to behaviour: A systematic review. Physiol Behav
1240 *167*, 341–353. https://doi.org/10.1016/j.physbeh.2016.09.030.

1241 89. Muzar, Z., Lozano, R., Kolevzon, A., and Hagerman, R.J. (2016). The neurobiology of the
1242 Prader-Willi phenotype of fragile X syndrome. Intractable Rare Dis Res *5*, 255–261.
1243 https://doi.org/10.5582/irdr.2016.01082.

1244 90. Long, J.-Y., Jiang, W., Xia, H.-B., Fu, J.-Y., Lu, P., Hu, F., Feng, W.-C., Sun, W.-W., Gao,
1245 M.-M., Yi, Y.-H., et al. (2020). FMRP-absence-induced up-regulation of hypothalamic
1246 MAP1B expression decreases AgRP level linking with reduces in food intake and body
1247 weight. Neurochem Int *140*, 104847. https://doi.org/10.1016/j.neuint.2020.104847.

1248 91. Sahoo, T., del Gaudio, D., German, J.R., Shinawi, M., Peters, S.U., Person, R.E., Garnica,
1249 A., Cheung, S.W., and Beaudet, A.L. (2008). Prader-Willi phenotype caused by paternal
1250 deficiency for the HBII-85 C/D box small nucleolar RNA cluster. Nat Genet *40*, 719–721.
1251 https://doi.org/10.1038/ng.158.

1252 92. Duker, A.L., Ballif, B.C., Bawle, E.V., Person, R.E., Mahadevan, S., Alliman, S.,
1253 Thompson, R., Traylor, R., Bejjani, B.A., Shaffer, L.G., et al. (2010). Paternally inherited
1254 microdeletion at 15q11.2 confirms a significant role for the SNORD116 C/D box snoRNA

1255 cluster in Prader-Willi syndrome. Eur J Hum Genet *18*, 1196–1201.
1256 https://doi.org/10.1038/ejhg.2010.102.

1257 93. Tan, Q., Potter, K.J., Burnett, L.C., Orsso, C.E., Inman, M., Ryman, D.C., and Haqq, A.M.
1258 (2020). Prader-Willi-Like Phenotype Caused by an Atypical 15q11.2 Microdeletion.
1259 Genes (Basel) *11*. https://doi.org/10.3390/genes11020128.

1260 94. Baldini, L., Robert, A., Charpentier, B., and Labialle, S. (2022). Phylogenetic and
1261 Molecular Analyses Identify SNORD116 Targets Involved in the Prader-Willi Syndrome.
1262 Mol Biol Evol *39*. https://doi.org/10.1093/molbev/msab348.

1263 95. Knott, B., Kocher, M.A., Paz, H.A., Hamm, S.E., Fink, W., Mason, J., Grange, R.W.,
1264 Wankhade, U.D., and Good, D.J. (2022). Dietary Conjugated Linoleic Acid Reduces Body
1265 Weight and Fat in Snord116(m+/p-) and Snord116(m-/p-) Mouse Models of Prader-Willi
1266 Syndrome. Nutrients *14*. https://doi.org/10.3390/nu14040860.

1267 96. Gaskill, B.N., Gordon, C.J., Pajor, E.A., Lucas, J.R., Davis, J.K., and Garner, J.P. (2013).
1268 Impact of nesting material on mouse body temperature and physiology. Physiol Behav
1269 *110–111*, 87–95. https://doi.org/10.1016/j.physbeh.2012.12.018.

1270 97. Gessulat, S., Schmidt, T., Zolg, D.P., Samaras, P., Schnatbaum, K., Zerweck, J., Knaute,
1271 T., Rechenberger, J., Delanghe, B., Huhmer, A., et al. (2019). Prosit: proteome-wide
1272 prediction of peptide tandem mass spectra by deep learning. Nat Methods *16*, 509–518.
1273 https://doi.org/10.1038/s41592-019-0426-7.

1274 98. Zhang, Y., Glineburg, M.R., Basrur, V., Conlon, K., Wright, S.E., Krans, A., Hall, D.A.,
1275 and Todd, P.K. (2022). Mechanistic convergence across initiation sites for RAN
1276 translation in fragile X associated tremor ataxia syndrome. Hum Mol Genet *31*, 2317–
1277 2332. https://doi.org/10.1093/hmg/ddab353.

1278 99. Huppertz, I., Attig, J., D'Ambrogio, A., Easton, L.E., Sibley, C.R., Sugimoto, Y., Tajnik,
1279 M., König, J., and Ule, J. (2014). iCLIP: Protein–RNA interactions at nucleotide
1280 resolution. Methods *65*, 274–287. https://doi.org/10.1016/j.ymeth.2013.10.011.

1281 100. Afgan, E., Baker, D., Batut, B., van den Beek, M., Bouvier, D., Cech, M., Chilton, J.,
1282 Clements, D., Coraor, N., Grüning, B.A., et al. (2018). The Galaxy platform for accessible,
1283 reproducible and collaborative biomedical analyses: 2018 update. Nucleic Acids Res *46*,
1284 W537–W544. https://doi.org/10.1093/nar/gky379.

1285 101. Heyl, F., Maticzka, D., and Batut, B. (2026). CLIP-Seq data analysis from pre-processing
1286 to motif detection (Galaxy Training Materials).

1287 102. Bolger, A.M., Lohse, M., and Usadel, B. (2014). Trimmomatic: a flexible trimmer for
1288 Illumina sequence data. Bioinformatics *30*, 2114–2120.
1289 https://doi.org/10.1093/bioinformatics/btu170.

1290 103. Dobin, A., Davis, C.A., Schlesinger, F., Drenkow, J., Zaleski, C., Jha, S., Batut, P.,
1291 Chaisson, M., and Gingeras, T.R. (2013). STAR: ultrafast universal RNA-seq aligner.
1292 Bioinformatics *29*, 15–21. https://doi.org/10.1093/bioinformatics/bts635.

1293 104. Tarasov, A., Vilella, A.J., Cuppen, E., Nijman, I.J., and Prins, P. (2015). Sambamba: fast
1294 processing of NGS alignment formats. Bioinformatics *31*, 2032–2034.
1295 https://doi.org/10.1093/bioinformatics/btv098.

1296 105. Liao, Y., Smyth, G.K., and Shi, W. (2014). featureCounts: an efficient general purpose
1297 program for assigning sequence reads to genomic features. Bioinformatics *30*, 923–930.
1298 https://doi.org/10.1093/bioinformatics/btt656.

1299 106. Smyth, G.K. (2005). Limma: linear models for microarray data. In: "Bioinformatics and
1300 Computational Biology Solutions using R and Bioconductor."

1301 107. Smedley, D., Haider, S., Ballester, B., Holland, R., London, D., Thorisson, G., and
1302 Kasprzyk, A. (2009). BioMart--biological queries made easy. BMC Genomics *10*, 22.
1303 https://doi.org/10.1186/1471-2164-10-22.

1304 108. Quinlan, A.R., and Hall, I.M. (2010). BEDTools: a flexible suite of utilities for comparing
1305 genomic features. Bioinformatics *26*, 841–842.
1306 https://doi.org/10.1093/bioinformatics/btq033.

1307 109. Li, Y., Aguilar-Martinez, E., and Sharrocks, A.D. (2019). Geno2proteo, a Tool for Batch
1308 Retrieval of DNA and Protein Sequences from Any Genomic or Protein Regions. J Integr
1309 Bioinform *16*, 20180090. https://doi.org/10.1515/jib-2018-0090.

1310 110. Peier, A.M., McIlwain, K.L., Kenneson, A., Warren, S.T., Paylor, R., and Nelson, D.L.
1311 (2000). (Over)correction of FMR1 deficiency with YAC transgenics: behavioral and
1312 physical features. Hum Mol Genet *9*, 1145–1159.

1313 111. Liu, Z.-H., Chuang, D.-M., and Smith, C.B. (2011). Lithium ameliorates phenotypic
1314 deficits in a mouse model of fragile X syndrome. Int J Neuropsychopharmacol *14*, 618–
1315 630. https://doi.org/10.1017/S1461145710000520.

1316 112. Pietropaolo, S., Guilleminot, A., Martin, B., D'Amato, F.R., and Crusio, W.E. (2011).
1317 Genetic-background modulation of core and variable autistic-like symptoms in Fmr1
1318 knock-out mice. PLoS One *6*, e17073. https://doi.org/10.1371/journal.pone.0017073.

1319 113. Ding, Q., Sethna, F., and Wang, H. (2014). Behavioral analysis of male and female Fmr1
1320 knockout mice on C57BL/6 background. Behav Brain Res *271*, 72–78.
1321 https://doi.org/10.1016/j.bbr.2014.05.046.

1322 114. Spencer, C.M., Alekseyenko, O., Serysheva, E., Yuva-Paylor, L.A., and Paylor, R. (2005).
1323 Altered anxiety-related and social behaviors in the Fmr1 knockout mouse model of fragile
1324 X syndrome. Genes Brain Behav *4*, 420–430. https://doi.org/10.1111/j.1601-
1325 183X.2005.00123.x.

1326 115. Gholizadeh, S., Arsenault, J., Xuan, I.C., Pacey, L.K., and Hampson, D.R. (2014).
1327 Reduced phenotypic severity following adeno-associated virus-mediated Fmr1 gene
1328 delivery in fragile X mice. Neuropsychopharmacology *39*, 3100–3111.
1329 https://doi.org/10.1038/npp.2014.167.

1330 116. Dahlhaus, R., and El-Husseini, A. (2010). Altered neuroligin expression is involved in
1331 social deficits in a mouse model of the fragile X syndrome. Behav Brain Res *208*, 96–105.
1332 https://doi.org/10.1016/j.bbr.2009.11.019.

1333 117. Mineur, Y.S., Sluyter, F., de Wit, S., Oostra, B.A., and Crusio, W.E. (2002). Behavioral
1334 and neuroanatomical characterization of the Fmr1 knockout mouse. Hippocampus *12*, 39–
1335 46. https://doi.org/10.1002/hipo.10005.

1336 118. Restivo, L., Ferrari, F., Passino, E., Sgobio, C., Bock, J., Oostra, B.A., Bagni, C., and
1337 Ammassari-Teule, M. (2005). Enriched environment promotes behavioral and
1338 morphological recovery in a mouse model for the fragile X syndrome. Proc Natl Acad Sci
1339 U S A *102*, 11557–11562. https://doi.org/10.1073/pnas.0504984102.

1340 119. Veeraragavan, S., Bui, N., Perkins, J.R., Yuva-Paylor, L.A., Carpenter, R.L., and Paylor,
1341 R. (2011). Modulation of behavioral phenotypes by a muscarinic M1 antagonist in a
1342 mouse model of fragile X syndrome. Psychopharmacology (Berl) *217*, 143–151.
1343 https://doi.org/10.1007/s00213-011-2276-6.

1344 120. Spencer, C.M., Alekseyenko, O., Hamilton, S.M., Thomas, A.M., Serysheva, E., Yuva-
1345 Paylor, L.A., and Paylor, R. (2011). Modifying behavioral phenotypes in Fmr1KO mice:
1346 genetic background differences reveal autistic-like responses. Autism Res *4*, 40–56.
1347 https://doi.org/10.1002/aur.168.

1348 121. Heulens, I., D'Hulst, C., Van Dam, D., De Deyn, P.P., and Kooy, R.F. (2012).
1349 Pharmacological treatment of fragile X syndrome with GABAergic drugs in a knockout
1350 mouse model. Behav Brain Res *229*, 244–249. https://doi.org/10.1016/j.bbr.2012.01.031.

1351 122. Paylor, R., Yuva-Paylor, L.A., Nelson, D.L., and Spencer, C.M. (2008). Reversal of
1352 sensorimotor gating abnormalities in Fmr1 knockout mice carrying a human Fmr1
1353 transgene. Behav Neurosci *122*, 1371–1377. https://doi.org/10.1037/a0013047.

1354 123. Baker, K.B., Wray, S.P., Ritter, R., Mason, S., Lanthorn, T.H., and Savelieva, K.V. (2010).
1355 Male and female Fmr1 knockout mice on C57 albino background exhibit spatial learning
1356 and memory impairments. Genes Brain Behav *9*, 562–574. https://doi.org/10.1111/j.1601-
1357 183X.2010.00585.x.

1358 124. Yan, Q.J., Asafo-Adjei, P.K., Arnold, H.M., Brown, R.E., and Bauchwitz, R.P. (2004). A
1359 phenotypic and molecular characterization of the fmr1-tm1Cgr fragile X mouse. Genes
1360 Brain Behav *3*, 337–359. https://doi.org/10.1111/j.1601-183X.2004.00087.x.

1361 125. Ventura, R., Pascucci, T., Catania, M.V., Musumeci, S.A., and Puglisi-Allegra, S. (2004).
1362 Object recognition impairment in Fmr1 knockout mice is reversed by amphetamine:
1363 involvement of dopamine in the medial prefrontal cortex. Behav Pharmacol *15*, 433–442.

1364 126. King, M.K., and Jope, R.S. (2013). Lithium treatment alleviates impaired cognition in a
1365 mouse model of fragile X syndrome. Genes Brain Behav *12*, 723–731.
1366 https://doi.org/10.1111/gbb.12071.

1367 127. McNaughton, C.H., Moon, J., Strawderman, M.S., Maclean, K.N., Evans, J., and Strupp,
1368 B.J. (2008). Evidence for social anxiety and impaired social cognition in a mouse model

1369 of fragile X syndrome. Behav Neurosci *122*, 293–300. https://doi.org/10.1037/0735-
1370 7044.122.2.293.

1371 128. Liu, Z.-H., and Smith, C.B. (2009). Dissociation of social and nonsocial anxiety in a
1372 mouse model of fragile X syndrome. Neurosci Lett *454*, 62–66.
1373 https://doi.org/10.1016/j.neulet.2009.02.066.

1374 129. Levenga, J., de Vrij, F.M., Buijsen, R.A., Li, T., Nieuwenhuizen, I.M., Pop, A., Oostra,
1375 B.A., and Willemsen, R. (2011). Subregion-specific dendritic spine abnormalities in the
1376 hippocampus of Fmr1 KO mice. Neurobiol Learn Mem *95*, 467–472.
1377 https://doi.org/10.1016/j.nlm.2011.02.009.

1378 130. Grossman, A.W., Elisseou, N.M., McKinney, B.C., and Greenough, W.T. (2006).
1379 Hippocampal pyramidal cells in adult Fmr1 knockout mice exhibit an immature-appearing
1380 profile of dendritic spines. Brain Res *1084*, 158–164.
1381 https://doi.org/10.1016/j.brainres.2006.02.044.

1382 131. Antar, L.N., Li, C., Zhang, H., Carroll, R.C., and Bassell, G.J. (2006). Local functions for
1383 FMRP in axon growth cone motility and activity-dependent regulation of filopodia and
1384 spine synapses. Mol Cell Neurosci *32*, 37–48. https://doi.org/10.1016/j.mcn.2006.02.001.

1385 132. Huber, K.M., Gallagher, S.M., Warren, S.T., and Bear, M.F. (2002). Altered synaptic
1386 plasticity in a mouse model of fragile X mental retardation. Proc Natl Acad Sci U S A *99*,
1387 7746–7750.

1388 133. Gross, C., Nakamoto, M., Yao, X., Chan, C.B., Yim, S.Y., Ye, K., Warren, S.T., and
1389 Bassell, G.J. (2010). Excess phosphoinositide 3-kinase subunit synthesis and activity as a
1390 novel therapeutic target in fragile X syndrome. J Neurosci *30*, 10624–10638.
1391 https://doi.org/10.1523/JNEUROSCI.0402-10.2010.

1392 134. Muddashetty, R.S., Kelić, S., Gross, C., Xu, M., and Bassell, G.J. (2007). Dysregulated
1393 metabotropic glutamate receptor-dependent translation of AMPA receptor and
1394 postsynaptic density-95 mRNAs at synapses in a mouse model of fragile X syndrome. J
1395 Neurosci *27*, 5338–5348. https://doi.org/10.1523/JNEUROSCI.0937-07.2007.

1396 135. Weiler, I.J., Spangler, C.C., Klintsova, A.Y., Grossman, A.W., Kim, S.H., Bertaina-
1397 Anglade, V., Khaliq, H., de Vries, F.E., Lambers, F.A., Hatia, F., et al. (2004). Fragile X
1398 mental retardation protein is necessary for neurotransmitter-activated protein translation
1399 at synapses. Proc Natl Acad Sci U S A *101*, 17504–17509.

1400 136. Volk, L.J., Pfeiffer, B.E., Gibson, J.R., and Huber, K.M. (2007). Multiple Gq-coupled
1401 receptors converge on a common protein synthesis-dependent long-term depression that
1402 is affected in fragile X syndrome mental retardation. J Neurosci *27*, 11624–11634.
1403 https://doi.org/10.1523/JNEUROSCI.2266-07.2007.

1404 137. Zeisel, A., Hochgerner, H., Lönnerberg, P., Johnsson, A., Memic, F., van der Zwan, J.,
1405 Häring, M., Braun, E., Borm, L.E., La Manno, G., et al. (2018). Molecular Architecture
1406 of the Mouse Nervous System. Cell *174*, 999-1014.e22.
1407 https://doi.org/10.1016/j.cell.2018.06.021.

138. Darnell, J.C., Fraser, C.E., Mostovetsky, O., Stefani, G., Jones, T.A., Eddy, S.R., and Darnell, R.B. (2005). Kissing complex RNAs mediate interaction between the Fragile-X mental retardation protein KH2 domain and brain polyribosomes. Genes Dev *19*, 903–918.

139. Hafner, M., Landthaler, M., Burger, L., Khorshid, M., Hausser, J., Berninger, P., Rothballer, A., Ascano, M., Jungkamp, A.-C., Munschauer, M., et al. (2010). Transcriptome-wide Identification of RNA-Binding Protein and MicroRNA Target Sites by PAR-CLIP. Cell *141*, 129–141. https://doi.org/10.1016/j.cell.2010.03.009.

Acknowledgments:

We thank Andrea Accogli (McGill U.), Vincenzo Salpietro Damiano (UCL Institute of Neurology, UK), SeSong Jang (Seoul U), Patrick Edry (Lyon U) for sharing data about DGKk variants. We are deeply grateful to Prof Jean-Louis Mandel for constant support throughout this project, Marie-Christine Birling and the members of the Institut Clinique de la Souris for their invaluable assistance in generating the *Dgkκ*-KO model and performing behavioral studies. We also acknowledge Bernard Jost and Stephanie Legras for their expert guidance on sequencing strategies and sequence analysis, Erwan Grandgirard for imaging support, and Bastien Morlet for his help with PRM studies. We are particularly indebted to Nicolas Charlet-Berguerand, Frank Martin, Juliette Godin, Albert Weixlbaumer for their insightful discussions and suggestions. Our sincere thanks go to Sirine Souali-Crespo for her support in anatomical studies and to Nicolas Zerbe and the IGBMC core facilities for their technical assistance. Finally, we thank our colleagues in the TMN department for their support and interest throughout this work.

Funding:

This work was supported by Fondation Jérôme Lejeune funding and StrasND to HM, by Fragile X France and APLM to OK and Fondation pour la Recherche Médicale to BZ. This study was also supported by ANR-10-LABX-0030-INRT under the frame program Investissements d'Avenir ANR-10-IDEX-0002-02.

Author contributions

OC, BZ, LN, GG designed and performed experiments and helped writing the manuscript. ND and AP performed experiments. AP helped designing the experiments and writing manuscript. TM and OC designed and performed bioinformatic analyses. HM supervised the project, designed and performed experiments and wrote the manuscript.

1443

1444 **Table 1. Summary of behavioral, cognitive, physiological, and cellular phenotypes of**
1445 ***Dgkk*-KO vs *Fmr1*-KO knockout mice (↓ decrease; ↑ increase;** ns **no**t significant ; ? unknown**)**
1446

Domain	**Fragile X syndrome clinical phenotype**	**Assay**	**Phenotype**	***Dgkk*KO**	***Fmr1*KO**	**references**
General Activity	Hyperactivity	Open field	Increased locomotor activity	↑	↑	11,28,110–118
Repetitive Behaviors	Perseveration and repetitive behaviors	Marble burying	Higher number of buried marbles	↑	↑	28,115,119,120
Anxiety	Increased anxiety	Elevated plus-maze	Open arm/closed arm	↑	↑	28,110,111,121
Sensorimotor Gating	Reduced prepulse inhibition	Prepulse inhibition	Enhanced prepulse inhibition; reduced startle response	↑	↑	112,113,119,120,122,123
Cognition	Intellectual disability, working memory deficits	Novel object recognition	No preference for novel object No genotype differences	ns	ns ↓	28,124 125,126
Social	Social phobia and avoidance	Three-chambered sociability task	No genotype differences No preference for novel mouse	ns	ns ↓	28,111,112,127,128 116,127
Physiology	Overgrowth	Weighing	Weight gain	↑	↑	62,86
		qNMR	Increased bone density	↑	↑	62
		qNMR	Increased lean/fat	↑	↑	62
	Macroorchidism	Testes size/weight	Macroorchidism	ns	↑	11
	Cardiopathy	Echocardiography	Left ventricular dilatation	↑	?	
Neuron morphology	Abnormal dendritic spines	Dendritic spine imaging	Abnormal dendritic spines	↑	↑	13,14,16,23,129–131
Neuron activity	hypersensitivity	Neuronal activity recording	Abnormal mGluR1 synaptic activity	↑	↑	132
	Abnormal DAG signaling	Phosphorylation status of DAG pathway	Abnormal DAG signaling	↑	↑	23,28
	Increased neuronal translation rate	Metabolic labelling	Increased translation rate	↑	↑	21,133–136

1447
1448
1449

1450 **Figure legends:**
1451
1452 **Figure 1: FMRP binds the m^{6}A modified EPAP motif of *Dgkκ* mRNA.**
1453 A) IGV representation of *Dgkκ* mRNA showing HITS-CLIP-seq profiles of FMRP (upper
1454 tracks) and m^{6}A-seq profiles (lower tracks) from hypothalamic neurons, relative to input [34].
1455 Sequence logo analysis of conserved FMRP binding sites in mouse and human DGKκ.
1456 B) CLIP-qPCR in HeLa cells for Ex1-DGKκ-Nluc and ΔEPAP-Nluc constructs. Bars represent
1457 IP/Input relative enrichment. A non-target control (GAPDH) was included to assess specificity.
1458 Each dot represents an independent culture.
1459 C) CLIP–qPCR analysis of FMRP in cortical neurons treated with Acell siRNA control or
1460 siRNA targeting *Mettl3*. Bars represent IP/Input enrichment relative to Map1b signal. Well-
1461 established FMRP targets (*Map1b*, *Psd95*), non-target controls (*Rplp0*), an m^{6}A-containing
1462 FMRP target (*Cdk5r1*), and a non-target (*Bdnf*) were included for specificity assessment. Each
1463 dot represents an independent culture. Data are mean ± SEM and analyzed using multiple t-
1464 tests comparing enrichment in WT and *Fmr1*-KO for each gene. **P < 0.01.
1465 D) RNA pull-down proteomic analysis using immobilized EPAP RNA probes with or without
1466 m^{6}A modification, incubated with WT neuronal lysate. P-values were calculated using a two-
1467 sided unpaired t test, and statistical thresholds for binding (dotted lines) were determined at 1
1468 standard deviation and P-value < 0.05.
1469 E) Schematic of the RNA nHU assay used to assess binding of EPAP RNA probes incubated
1470 with WT or *Fmr1*-KO neuronal lysates. Probes were incubated with lysates at concentrations
1471 ranging from 0 to 2.5 μM. Binding index (BI) values were analyzed by non-linear regression
1472 fitting to bimolecular binding equations.
1473
1474
1475 **Figure 2: FMRP and m6A mitigates ribosomal stalling imposed by the EPAP repeats.**
1476 A) Representative western blot of transfected WT DGKκ and ΔNter DGKκ tagged with HA in
1477 HeLa cells. GAPDH was used as a loading control.
1478 B) Translation efficiency measurements of the indicated constructs in HeLa cells. Luciferase
1479 signals were normalized to RNA levels of the corresponding constructs.
1480 C–D) Sucrose gradient control shows ribosome profile of undigested and RNase-A-digested
1481 lysate. Northern blot analysis of RNase-A–digested ribosomal footprints. Specific radio-labeled
1482 probes for NLuc (C-D) and EPAP (D) were used. For emetine-positive control, cells were
1483 incubated with 2 μM emetine for 15 min prior to lysis. Ethidium bromide staining was used as
1484 a loading control.
1485 E) Luciferase assays of indicated NLuc constructs in WT and *Fmr1*-KO cortical primary
1486 neurons at DIV4. Firefly luciferase was used as a normalization control. Data are mean ± SEM
1487 and analyzed using multiple t-tests comparing enrichment in WT and *Fmr1*-KO for each gene.
1488 ***P < 0.001.
1489 F) Translation efficiency measurement of indicated constructs in HeLa cells transfected with
1490 control or *METTL3*-targeting siRNA. Luciferase signals were normalized to RNA levels of the
1491 corresponding constructs. Data are mean ± SEM and analyzed using multiple t-tests comparing
1492 enrichment in WT and *Fmr1*-KO for each gene. *P<0.05; ***P < 0.001.
1493
1494 **Figure 3: FXRs bind *Dgkκ* mRNA across the brain and display redundant function to**
1495 **regulate its translation**
1496 A) Single-molecule–resolution spatial transcriptomic MERFISH data (Vizgen) showing *Dgkκ*
1497 mRNA (blue) in mouse brain coronal sections. Upper panel: 3D reconstruction generated from
1498 67 MERFISH sections.

B) Single-cell transcriptomic [137] reanalysis showing the expression patterns of DGKs across major brain cell types.
C) qRT–PCR analysis of *Dgkκ* expression in cortex, hippocampus, hypothalamus, thalamus, pituitary gland, and pons from adult WT and *Fmr1*-KO mice. Fold changes were calculated using the ΔΔCt method with Tbp as the housekeeping gene. Data are mean ± SEM and were analyzed using multiple t-tests comparing expression in WT and *Fmr1*-KO across brain regions.
D) PRM-targeted proteomic quantification of DGKκ in cortex and hypothalamus from WT and *Fmr1*-KO mice. Each dot represents an individual mouse. Data are mean ± SEM and were analyzed using an unpaired Student's t-test. **P < 0.01, ***P<0.001.
E–F) CLIP–qPCR analysis of FMRP in primary E) cortical and F) hypothalamic neurons at DIV8. Bar graphs represent IP/Input enrichment relative to the Map1b signal. Established FMRP mRNA targets (*Map1b* and *Psd95*) and a non-target control (*Rplp0*) were included to assess specificity. Analysis in *Fmr1*-KO neurons confirms immunoprecipitation specificity. Each dot represents an independent culture.
G) Representative western blots of FMRP and FXR1P in cortex and hypothalamus. Quantification was normalized to GAPDH and expressed relative to cortex expression. Data are mean ± SEM and were analyzed using unpaired Student's t-tests. **P < 0.01.
H) CLIP–qPCR analysis of FXR1P in primary hypothalamic neurons at DIV8. Bar graphs represent IP/Input enrichment relative to the Map1b signal. An established FXR1P target (*cMyc*) was used as a positive control, while Rplp0 and Actb served as non-target controls.

Figure 4: *Dgkκ*-KO mice exhibit FXS-like and overgrowth phenotypes.
A) Body weight of WT and *Dgkκ*-KO mice measured across multiple ages, with representative images of WT and *Dgkκ*-KO mice (scale bar, 1 cm). Data are presented as median with interquartile range with minimum and maximum values and analyzed by two-way repeated-measures ANOVA to evaluate the overall effect of genotype. ***P < 0.001.
B-F) Quantitative NMR (qNMR) body composition analysis showing B) lean mass, C) free body fluid mass D), fat mass, E) body size measurements, F) bone density.
G, H) Echocardiographic assessment of G) heart mass and H) left ventricular mass. Each dot represents one mouse. Data are medians with interquartile range with minimum and maximum values and were analyzed using unpaired Student's t-tests. **P<0.01; ***P<0.001. I-J) Open field test. I, total distance traveled over 30 min and J, percentage of time spent in the center of the arena. K) Marble burying test. Number of marbles buried within 15 min, indicative of compulsive-like behavior and/or hyperactivity. Data are presented as median with interquartile range with minimum and maximum values and analyzed by unpaired Student's t-tests. *P<0.05.
L) Digging behavior measurement.
M) Social interaction test. Frequency of interactions between the test mouse and a novel conspecific.
N) Elevated plus maze test. Percentage of time spent in open arms, reflecting anxiety-like behavior.
O) Acoustic startle response. Amplitude of the startle reflex elicited by an acoustic stimulus.
B-0) Each dot represents one mouse. Data are represented as median with interquartile range with minimum and maximum values and were analyzed using unpaired Student's t-tests, *P<0.05, **P<0.001, ***P < 0.001.

Figure 5: DGKκ loss results in dendritic spines morphology and mGluRI-dependent activity alterations, and aberrant DAG-signaling leading to increased neuronal translational rate
A) Neuronal localization of HA-DGKκ (fire) in primary hippocampal neurons and its colocalization with the synaptic marker PSD95 (green) at 17 DIV. Hippocampal neurons were

magnetofected at 3 DIV with HA-tagged DGKκ constructs. At 17 DIV, neurons were immunolabeled with antibodies against HA and PSD95. Images were acquired by confocal microscopy. Digital magnification shows colocalization of DGKκ with PSD95 in dendritic spines. CB: cell body; Sp: spine. Scale bar: 30 µm.

B) Ribopuromycylation assay in hippocampal neurons at DIV17. Top panel: no puromycin control. Bottom panel: arrows indicate colocalization of DGKκ (fire) with puromycin signal (white), highlighting sites of active translation. Scale bar: 2 µm.

C) Quantification and classification of dendritic spine morphology in magnetofected GFP-positive hippocampal neurons at 21 DIV from WT and *Dgkκ*-KO mice. Upper panel: representative 3D reconstructions of dendritic spine morphology for each condition. Spine analysis was performed using Imaris on GFP-labeled neurons, analyzing 100–200 spines per 8–10 neurons per biological replicate. Each colored dot represents an individual culture. Data are presented as mean ± SEM and analyzed using two-way ANOVA followed by Sidak's multiple-comparisons test. *P < 0.05; **P < 0.01.

D) MEA recordings. Upper panel: raster plot example in which each line represents a different electrode (subset shown) and each dot represents an above-threshold spiking event. Lower panel: mGluRI-dependent activity in WT and *Dgkκ*-KO cortical neurons measured before and after 1 min of treatment with 100 µM DHPG. Each dot represents data from an individual embryo. Data are mean ± SEM and analyzed using paired Student's t-test. *P < 0.05; **P < 0.01.

E) Representative western blots of lysates from WT and *Dgkκ*-KO cortical neurons at 7 DIV and quantification of phosphorylation and total levels of indicated proteins. GAPDH was used as a loading control. Phospho-protein signals were normalized to total protein and expressed relative to WT. Data are mean ± SEM and were analyzed using unpaired Student's t-tests. **P<0.01; ****P<0.0001.

F) Representative western blots of puromycin-labeled neuron lysates from WT and *Dgkκ*-KO cortical neurons treated for 30 min with 20 µg/mL puromycin. Puromycin signals were normalized to GAPDH and expressed relative to WT. Each dot represents an individual culture. Data are mean ± SEM and were analyzed using unpaired Student's t-tests. **P<0.01.

Supplementary figure legends:

Figure S1: FMRP preferentially binds repetitive m⁶A-modified coding sequences and regulates DGKκ translation

A) Validation of FMRP immunoprecipitation in cortical neurons using an FMRP-specific antibody. *Fmr1*-KO neurons and IgG antibodies were used as negative controls.

B) qRT–PCR analysis of *Dgkκ* expression in primary cortical and hypothalamic neurons at DIV8. Relative expression levels were calculated using the ΔΔCT method with *Rplp0* as the housekeeping gene. Data are presented as mean ± SEM and were analyzed using an unpaired Student's t-test. ****P < 0.0001.

C) IGV representation of *Fmr1* (top panel) and *Rplp0* (bottom panel) mRNAs showing HITS-CLIP-seq profiles of FMRP relative to input.

D) Venn diagram illustrating the overlap between mRNA targets identified in this FMRP CLIP study and targets reported in two independent published datasets [25,138]. Shared and study-specific targets are indicated. For the [25] CLIP study, the FMRP target list was restricted to mRNAs containing more than one FMRP peak and supported by at least 50 reads.

E) iCLIP-seq (individual-nucleotide resolution UV crosslinking and immunoprecipitation) [99] allows identification of WT-specific RT-stop events downstream of EPAP that were absent in both *Fmr1*-KO and input RNA samples. IGV screenshot of FMRP iCLIP-seq data on *Dgkκ*

mRNA. The red box highlights a WT-specific peak corresponding to a truncation event indicative of an FMRP binding site, as predicted based on iCLIP read-through profiles [139].
F) AlphaFold-predicted structure of human DGKκ, highlighting the intrinsically disordered region corresponding to the EPAP domain.
G) qRT-PCR analysis of *Mettl3* expression in cortical neurons treated at DIV5 for 72 h with Accell control siRNA or siRNA targeting *Mettl3*. Fold changes were calculated using the ΔΔCT method with ActB as the housekeeping gene. Data are mean ± SEM and were analyzed using multiple t-tests. ****P < 0.0001.
H) qRT-PCR analysis of the indicated genes in cortical neurons treated at DIV5 for 72 h with Accell control siRNA or siRNA targeting *Mettl3*. Fold changes were calculated using the ΔΔCT method with *ActB* as the housekeeping gene. Data are mean ± SEM and analyzed using multiple t-tests comparing expression in siControl and si*Mettl3* conditions for each gene. *P<0.05.
I) EMSA using purified human His-tagged FMRP isoform 1 and radiolabeled EPAP RNA probes with or without m^6A modification.
J) IGV representation of *Dgkκ* mRNA showing RIP-seq profiles of YTHDF proteins in hippocampal neurons [42].
K) qRT-PCR analysis of cytosolic and nuclear RNA fractions to assess mRNA nuclear export of the indicated genes in WT and *Fmr1*-KO brain tissue. *U2* snRNA was used as a non-exported nuclear control.
L) qRT-PCR analysis of neurite and soma fractions to assess mRNA transport in WT and *Fmr1*-KO cortical neurons. *Gng3* was used as a poorly transported control mRNA and *Col3a1* as a highly neurite-enriched control.

Figure S2: m^6A modification in the EPAP repeats regulates DGKκ translation
A) qRT-PCR analysis in HeLa cells co-transfected for 24 h with the indicated constructs and control siRNA or siRNA targeting *METTL3*. GAPDH was used as the housekeeping gene. Data are mean ± SEM and analyzed using multiple t-tests comparing expression in siControl and si*METTL3* conditions for each gene. *P<0.05; **P<0.01.
B) Dot blot analysis using an anti-m^6A antibody on 1 µg of poly(A)+ RNA isolated from HeLa cells treated with DMSO or 20 µM STM2457 for 24 h. Methylene blue staining was used as a loading control. Representative western blots of HA-tagged constructs expressed in HeLa cells treated with increasing concentrations of STM2457 for 24 h are shown. GAPDH was used as a loading control.
C) qRT-PCR analysis of Nluc mRNA in HeLa cells transfected for 24 h with control siRNA or siRNA targeting *YTHDF1* or *YTHDF2*. GAPDH was used as the housekeeping gene. Translation efficiency of Ex1-DGKκ–NLuc was measured by normalizing luciferase activity to RNA levels of the corresponding construct. Data are presented as mean ± SEM and analyzed by one-way ANOVA with comparison to the siControl condition. *P < 0.05.

Figure S3: FXRs expression across the brain
A) PRM-targeted proteomic quantification of DGKκ in primary cortical neurons at DIV7 from WT and *Fmr1*-KO mice. Each dot represents an individual culture. Data are mean ± SEM and were analyzed using an unpaired Student's t-test. **P < 0.01.
B) PRM-targeted proteomic quantification of DGKκ in cortex and hypothalamus from WT and *Fmr1*-KO mice. Each dot represents an individual mouse. Data are mean ± SEM and were analyzed using an unpaired Student's t-test. **P < 0.01, ***P<0.001.
C) Expression pattern of FXR proteins in the mouse brain. Data obtained from www.proteinatlas.org.

1649 **Figure S4: Behavioral analyses and echocardiography of *Dgkκ*-KO mice**
1650 A) RT-PCR analysis of exons 1–4 and 8–9 of the *Dgkκ* gene in WT and *Dgkκ*-KO mice. *Gapdh*
1651 RT-PCR was used as a loading control.
1652 B) Western blot of hypothalamic lysates from WT and *Dgkκ*-KO mice using a partially DGKκ-
1653 specific antibody.
1654 C–D) Detection and quantification of a DGKκ-specific peptide by targeted proteomics in
1655 hypothalamic lysates from WT and *Dgkκ*-KO mice. C, representative detection. D,
1656 Quantification of DGKκ-specific peptide levels.
1657 E) qRT-PCR analysis of 9 Dgk isoforms and *Psd95* in WT and *Dgkκ*-KO mouse brains. Data
1658 are presented as mean fold change ± SEM and analyzed using unpaired Student's t-test.
1659 ***P<0.001.
1660 F–G) Echocardiography measurement of left ventricular blood volume during diastole (F) and
1661 systole (G).
1662 H) Social interaction test. Number of interactions between the test mouse and a novel
1663 conspecific.
1664 I) Elevated plus maze test. Measure of open arms and closed arms in a "+"-shaped maze. Total
1665 arm entries were counted to assess general locomotor activity.
1666 J) Novel object recognition test. Exploration duration during the habituation, acquisition, and
1667 retention phases. Recognition index was calculated to assess episodic memory.
1668 K) Nest-building assay. Nests were scored at 2, 5, and 24 h using a 0–5 scale as described by
1669 [96]: 0 = undisturbed nesting material; 1 = disturbed material but no nest site; 2 = flat nest without
1670 walls; 3 = cup nest with wall < ½ the height of a dome; 4 = incomplete dome with wall ½ the
1671 height of a dome; 5 = complete dome with walls > ½ the height of a dome, which may or may
1672 not fully enclose the nest.
1673 L) Social memory (percentage of exploration of a novel vs familiar congener).
1674 F-K) Each dot represents an individual mouse. Data are mean as median with interquartile range
1675 with minimum and maximum values and were analyzed using an unpaired Student's t-test. *P
1676 < 0.05. L) Data are expressed as median with interquartile range with minimum and maximum
1677 values and analyzed using one group t-test. ### p<0.0001 vs chance (50%).
1678
1679 **Figure S5: DGKκ regulates translation and neuronal electrical activity**
1680 A) Ribopuromycylation assay in hippocampal neurons. Top panel: no puromycin control.
1681 Middle panel: neurons pre-treated with 1.6 mM cycloheximide prior to ribopuromycylation to
1682 verify that puromycin signal is translation-specific. Bottom panel: ribopuromycylation signal.
1683 B) Number of active units recorded on MEA chips over time, reflecting neuronal activity from
1684 7 DIV to 35 DIV.
1685 C) Representative raw signal showing action potentials at basal level and during spontaneous
1686 bursting activity on a single electrode.
1687 D) Western blot analysis of lysates from WT and *Dgkκ*-KO hypothalamic neurons at 7 DIV,
1688 showing total and phosphorylated S6 protein. GAPDH was used as a loading control.
1689 Quantification: phospho-S6 signal normalized to total S6 and expressed relative to WT. Each
1690 dot represents an independent culture. Data are mean ± SEM and analyzed using unpaired
1691 Student's t-test. *P < 0.05.
1692
1693 **Figure S6: Functional impact of DGKk variants identified in individuals with NDD.**
1694 A) DGKk domains and location of the identified missense variants.
1695 B) Representative western blot of overexpressed DGKk variants found in patients with ID.
1696 Quantifications of the HA-DGKk signal were normalized against GAPDH protein signal and
1697 are presented relative to the WT.

C) Cellular localization of DGKk and impact of patient variants on its membrane localization. HeLa cells were transfected with the indicated constructs. DGKk catalytic domain deletion and benign mutation constructs were used respectively as a positive and negative controls. The histogram represents the signal intensity ratio membrane/cytosol obtained by measuring the signal intensity of a line passing through the cytosol (as indicated). A total of 100 cells from 3 different different cultures were counted and represented with different color symbols for each culture. Scale bar: 10 µM.

D) Neuronal localization of DGKk and impact of patient variants on its dendritic localization. Neurons were magnetofected at 3DIV and fixed at 8DIV. DGKk catalytic domain deletion and benign variant constructs were used as positive and negative controls, respectively. The quantification indicates the signal intensity ratio dendrite/soma over a distance of 120 µM. A total of 12 to 16 neurons from 3-4 cultures were quantified for each condition. Scale bar: 20 µM. Data are mean ± SEM.

Figure S7: FMRP mostly binds sequences coding for stalling-prone sequences

A) Frequency of amino acids encoded by sequences enriched in FMRP HITS-CLIP-seq targets relative to their frequency in the mouse proteome.

B) Hydrophobicity versus frequency of enriched tripeptides identified in FMRP-bound peptide sequences. Scatter plot showing the enrichment of unordered tripeptide motifs detected in amino-acid sequences derived from FMRP CLIP–enriched transcripts. Tripeptides were scanned in sliding windows of 30 amino acids, and motifs detected ≥2 times within the same window were collapsed into non-ordered compositions (e.g., EPE/PEE/EEP → "EEP"). The y-axis reports the fraction of enriched windows containing each motif across all FMRP-associated sequences. The x-axis shows the mean Kyte–Doolittle hydrophobicity, plotted on an inverted scale to distinguish hydrophobic (left) from hydrophilic (right) motifs; the dashed vertical line marks hydrophobicity 0. Point color indicates net charge (K/R: +1; D/E: –1), and selected motifs with high co-occurrence or extreme hydrophobicity are labelled.

C) Correlation between amino acid composition and m^6A consensus density. Each data point represents a genomic peak from the EPAP dataset. The x-axis shows the cumulative proportion of P, D, E, K, R, and Q amino acids within the protein sequence encoded by each peak, and the y-axis displays the number of m^6A motif per peak.

D) Proposed model for the coordinated action of FMRP and m^6A on amino acid clusters altering translational elongation process.

Figure 1

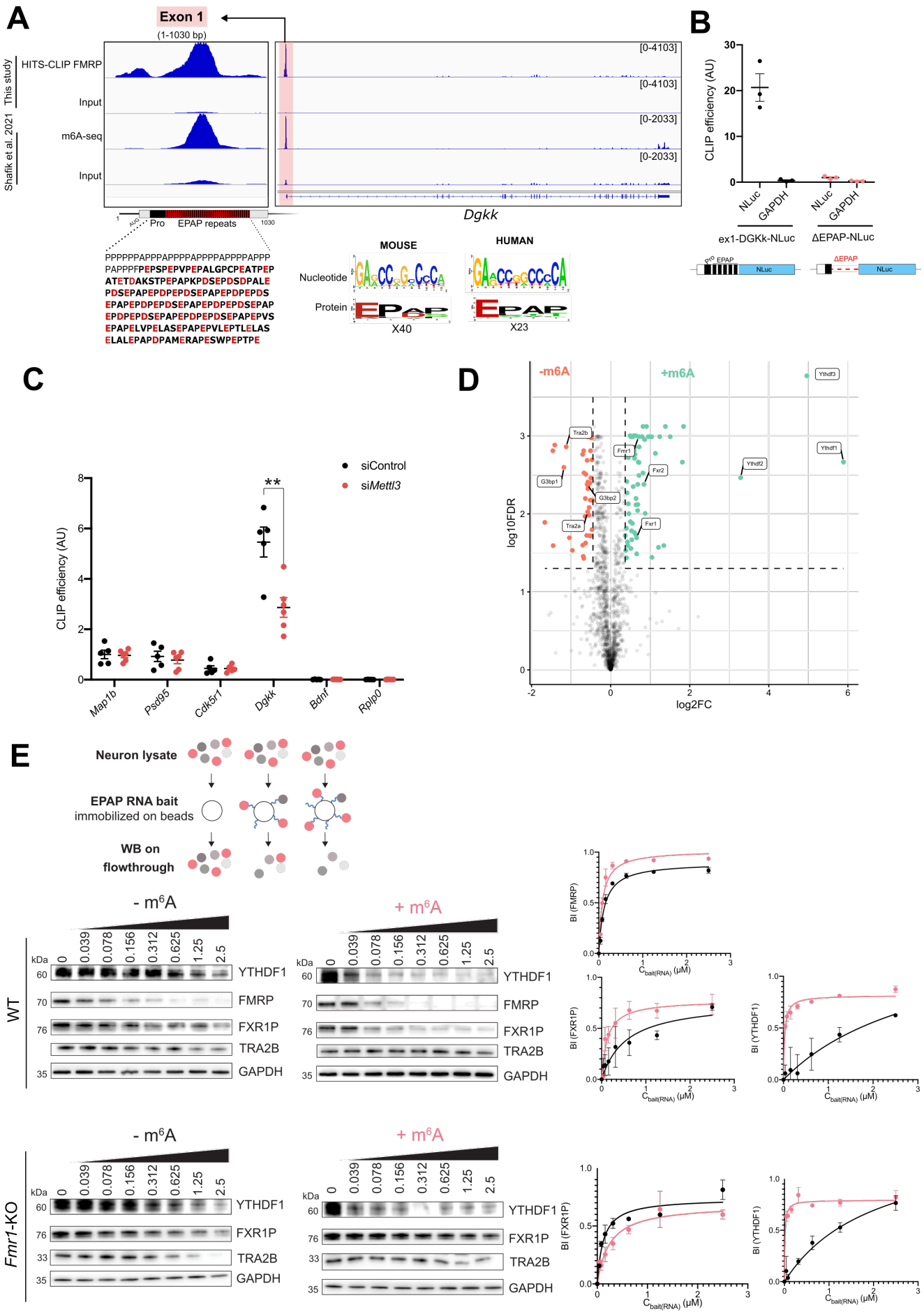
A
Exon 1
(1-1030 bp)
This study
HITS-CLIP FMRP
Input
Shafik et al. 2021
m6A-seq
Input
[0-4103]
[0-4103]
[0-2033]
[0-2033]
Pro
EPAP repeats
Dgkk
PPPPPPAPPPAPPPPAPPPPAPPPPAPPP
PAPPPFPEPSPEPVPEPALGPCPEATPEP
ATETDAKSTPEPAPKPDSEPDSDPALE
PDSEPAPEPDPEPDSEPAPEPDPEPDS
EPAPEPDPEPDSEPAPEPDPEPDSEPAP
EPDPEPDSEPAPEPDPEPDSEPAPEPVS
EPAPELVPELASEPAPEPVLEPTLELAS
ELALEPAPDPAMERAPESWPEPTPE
MOUSE
HUMAN
Nucleotide
Protein
X40
X23
B
CLIP efficiency (AU)
NLuc
GAPDH
ex1-DGKk-NLuc
ΔEPAP-NLuc
EPAP
ΔEPAP
C
CLIP efficiency (AU)
siControl
siMettl3
**
Map1b
Psd95
Cdk5r1
Dgkk
Bdnf
Rplp0
D
-m6A
+m6A
Ythdf3
Tra2b
Fmr1
Ythdf1
Ythdf2
Fxr2
G3bp1
G3bp2
Tra2a
Fxr1
log10FDR
log2FC
E
Neuron lysate
EPAP RNA bait
immobilized on beads
WB on
flowthrough
- m6A
+ m6A
0
0.039
0.078
0.156
0.312
0.625
1.25
2.5
kDa
YTHDF1
FMRP
FXR1P
TRA2B
GAPDH
WT
Fmr1-KO
BI (FMRP)
BI (FXR1P)
BI (YTHDF1)
C bait(RNA) (μM)

Figure 2

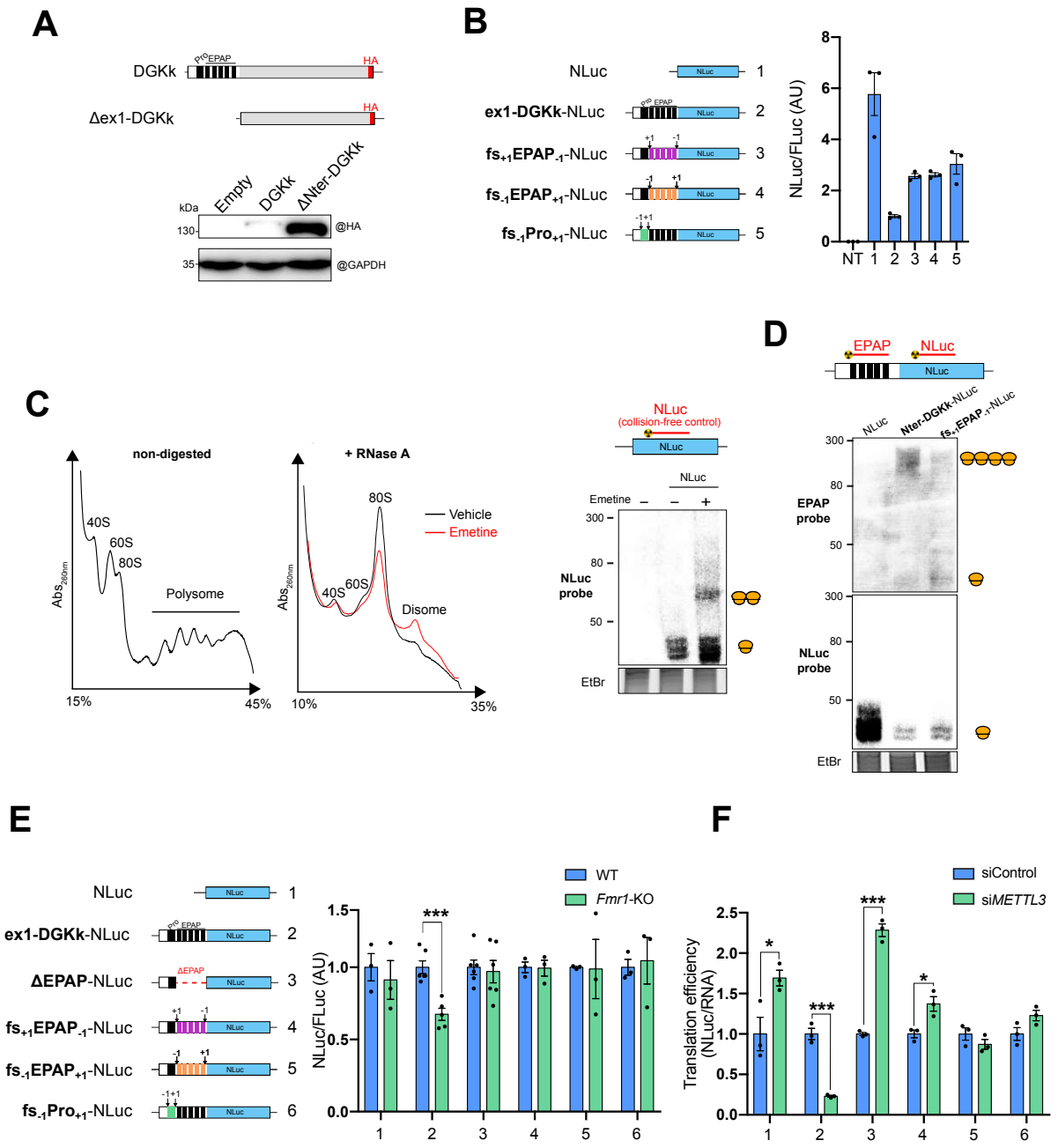

1735

1736

Figure 3

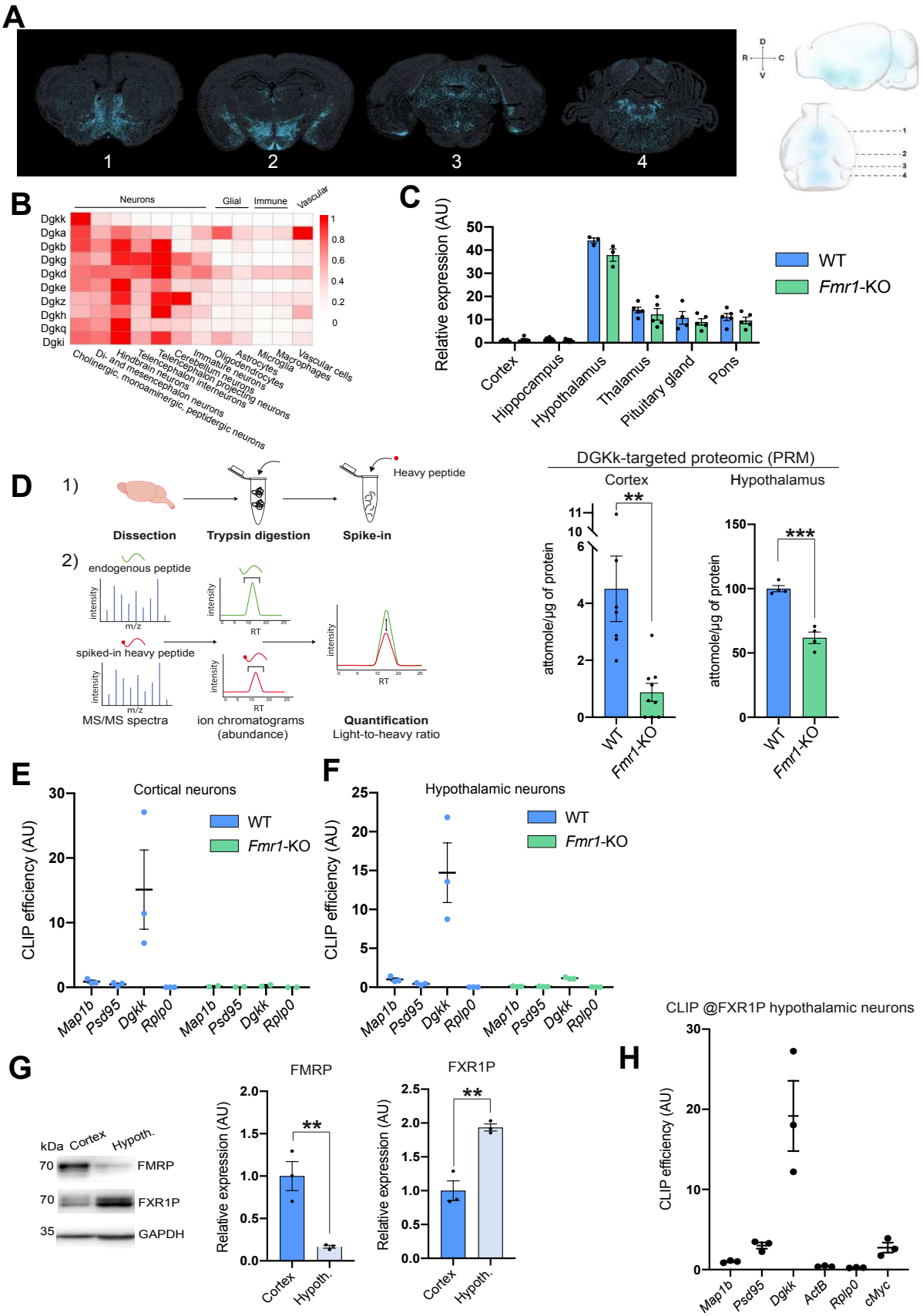
A
1
2
3
4
B
Neurons
Glial
Immune
Vascular
Dgkk
Dgka
Dgkb
Dgkg
Dgkd
Dgke
Dgkz
Dgkh
Dgkq
Dgki
Cholinergic, monoaminergic, peptidergic neurons
Di- and mesencephalon neurons
Hindbrain neurons
Telencephalon neurons
Telencephalon projecting neurons
Cerebellum neurons
Immature neurons
Oligodendrocytes
Astrocytes
Microglia
Macrophages
Vascular cells
C
Relative expression (AU)
WT
Fmr1-KO
Cortex
Hippocampus
Hypothalamus
Thalamus
Pituitary gland
Pons
D
1)
Dissection
Trypsin digestion
Heavy peptide
Spike-in
2)
endogenous peptide
spiked-in heavy peptide
MS/MS spectra
ion chromatograms
(abundance)
Quantification
Light-to-heavy ratio
DGKk-targeted proteomic (PRM)
Cortex
Hypothalamus
attomole/µg of protein
E
Cortical neurons
CLIP efficiency (AU)
Map1b
Psd95
Dgkk
Rplp0
F
Hypothalamic neurons
G
kDa
Cortex
Hypoth.
FMRP
FXR1P
GAPDH
Relative expression (AU)
H
CLIP @FXR1P hypothalamic neurons
ActB
cMyc

Figure 4

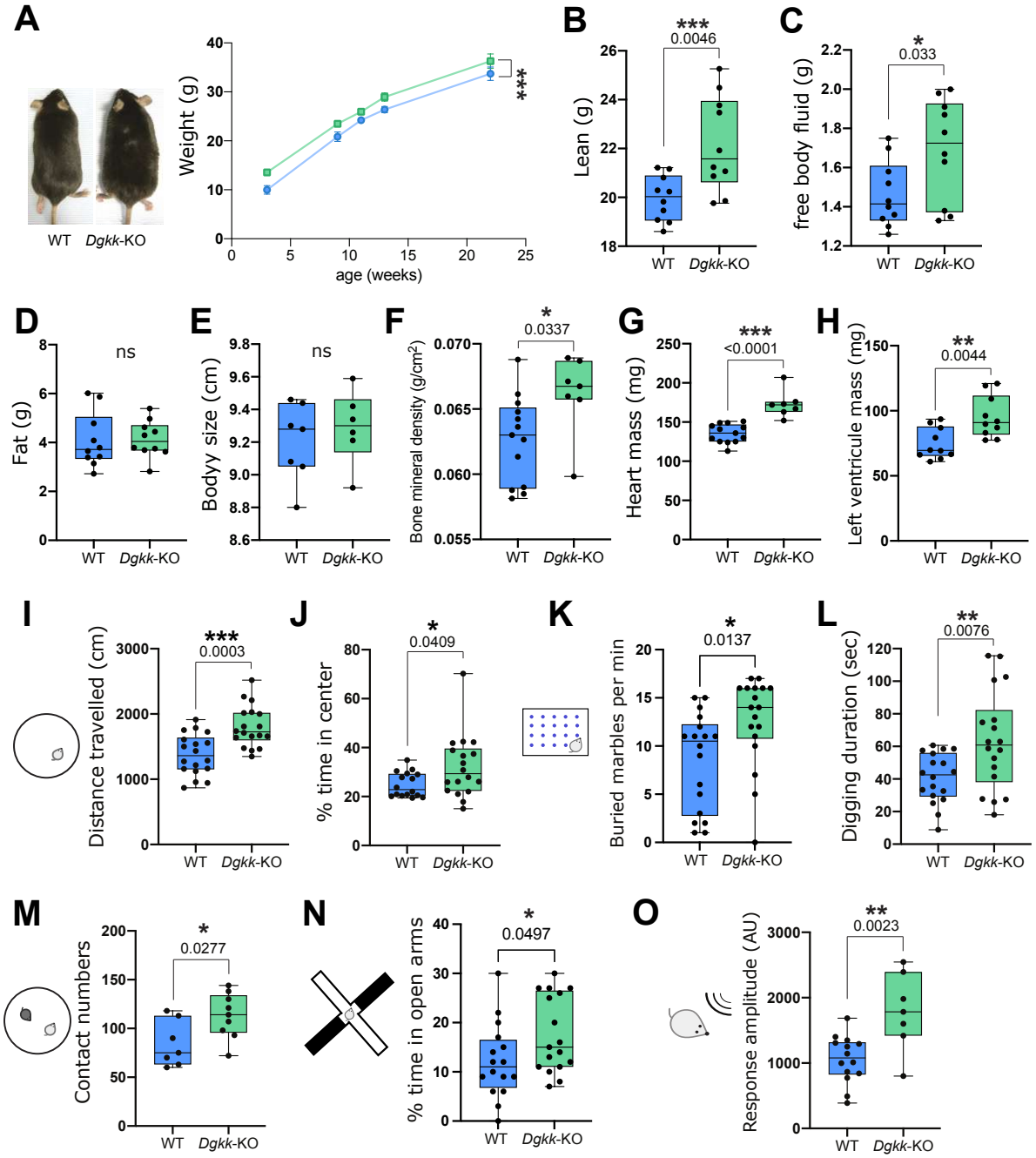

1740

1741

1742

Figure 5

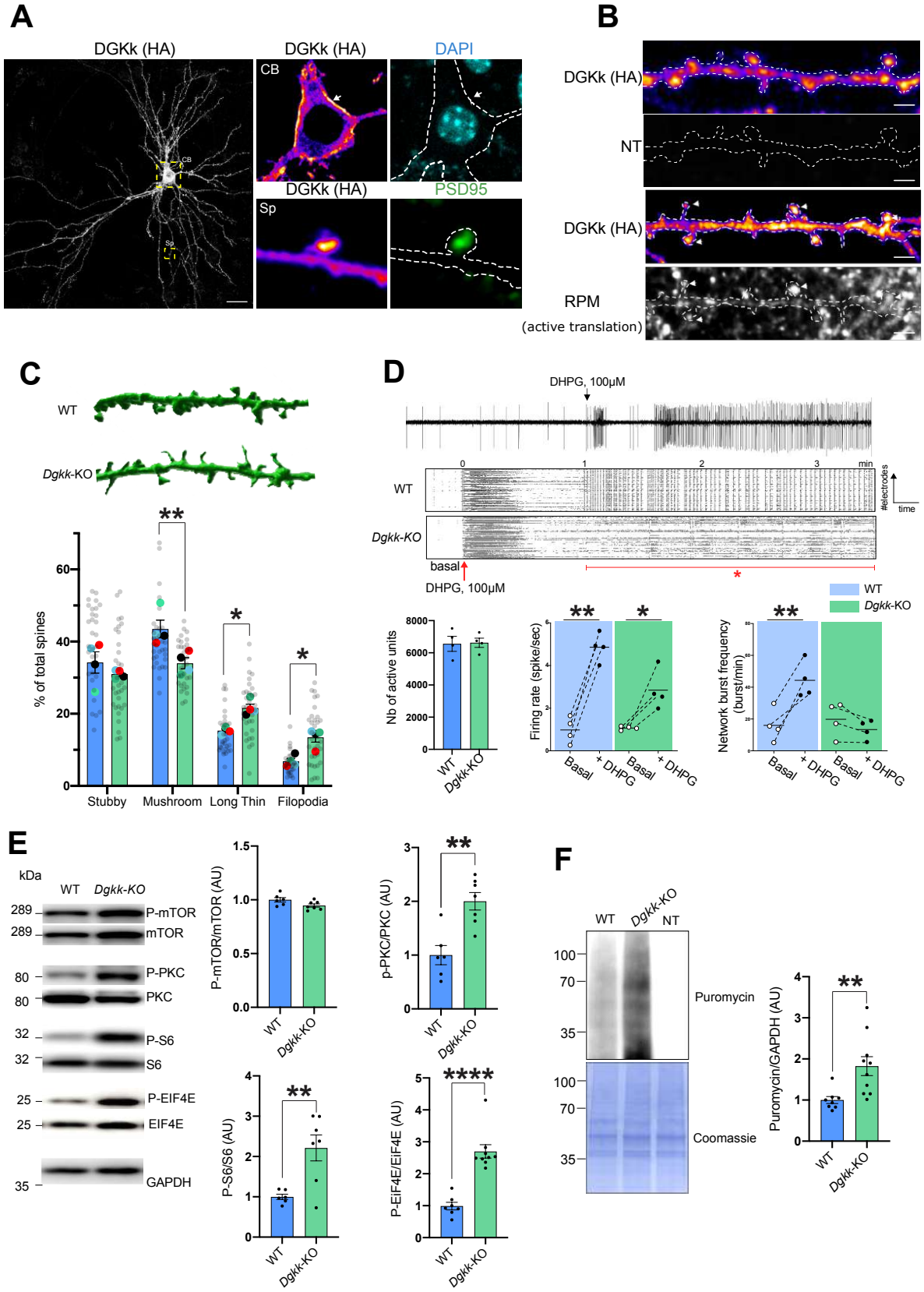
A
DGKk (HA)
DGKk (HA)
DAPI
CB
DGKk (HA)
PSD95
Sp
B
DGKk (HA)
NT
DGKk (HA)
RPM
(active translation)
C
WT
Dgkk-KO
% of total spines
Stubby
Mushroom
Long Thin
Filopodia
D
DHPG, 100μM
WT
Dgkk-KO
basal
DHPG, 100μM
#electrodes
time
Nb of active units
Firing rate (spike/sec)
Network burst frequency (burst/min)
Basal
+ DHPG
E
kDa
WT
Dgkk-KO
P-mTOR
mTOR
P-PKC
PKC
P-S6
S6
P-EIF4E
EIF4E
GAPDH
P-mTOR/mTOR (AU)
p-PKC/PKC (AU)
P-S6/S6 (AU)
P-EIF4E/EIF4E (AU)
F
WT
Dgkk-KO
NT
Puromycin
Coomassie
Puromycin/GAPDH (AU)

Supplementary Figure 1

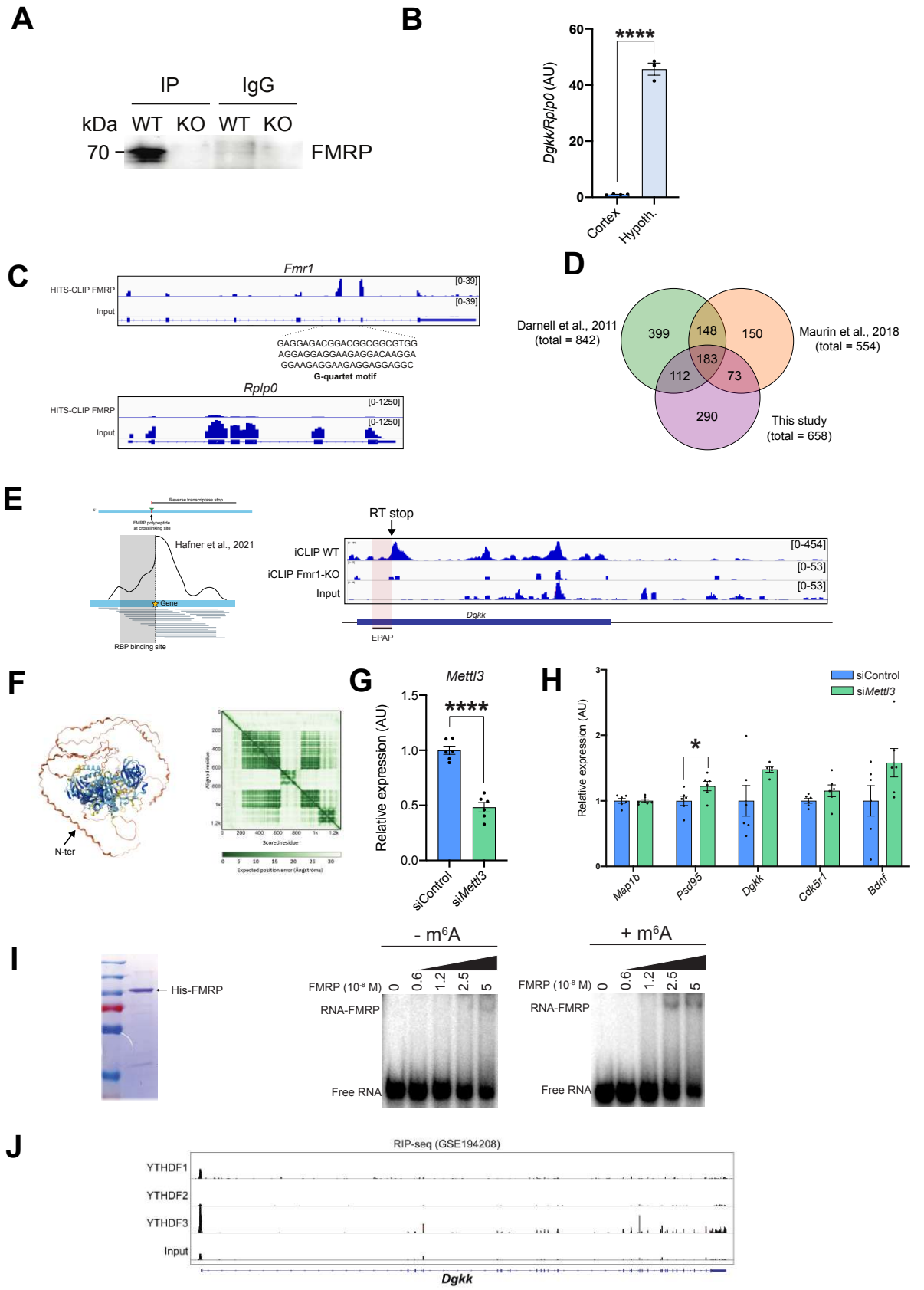

1746

1747

Supplementary Figure 1

K

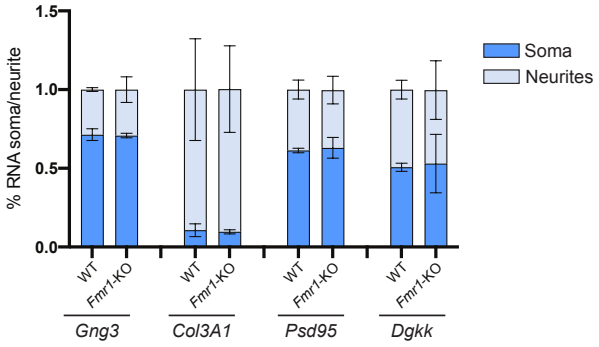

L

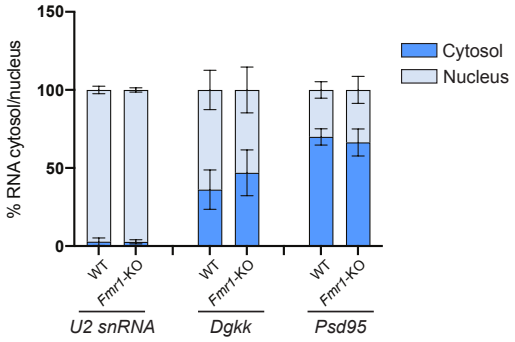

1748

Supplementary Figure 2

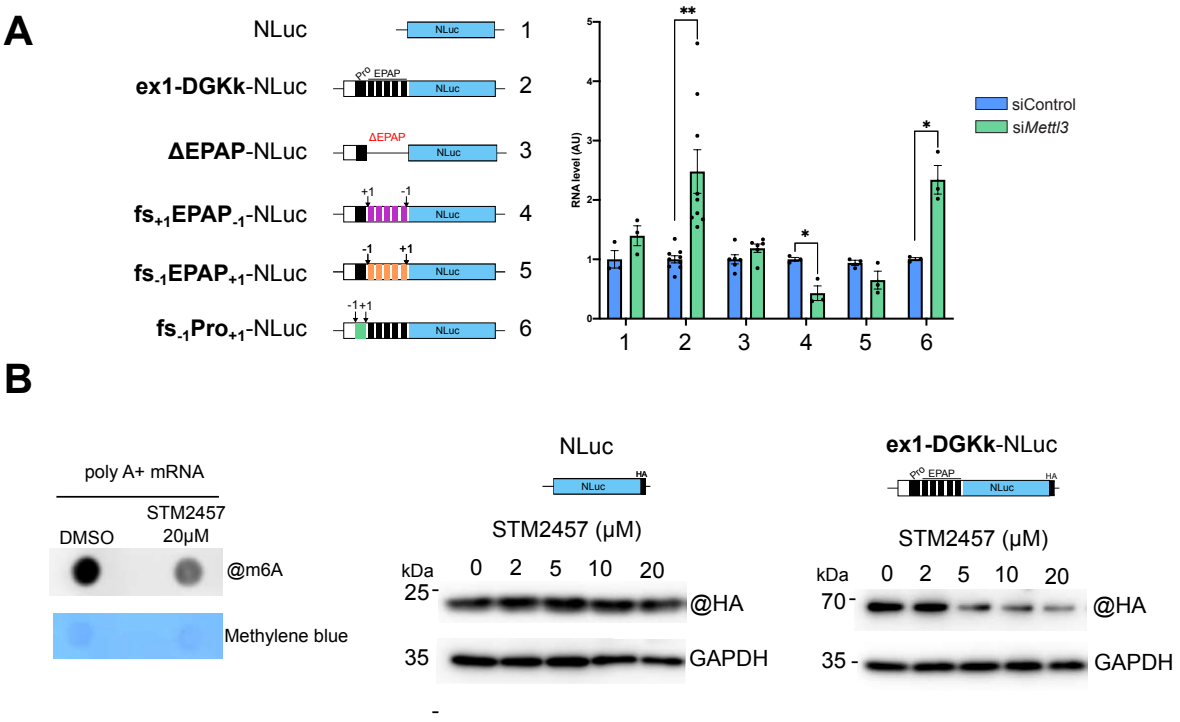

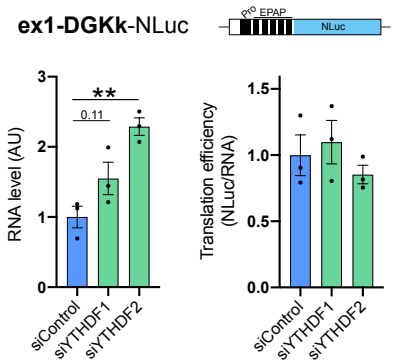

1749

Supplementary Figure 3

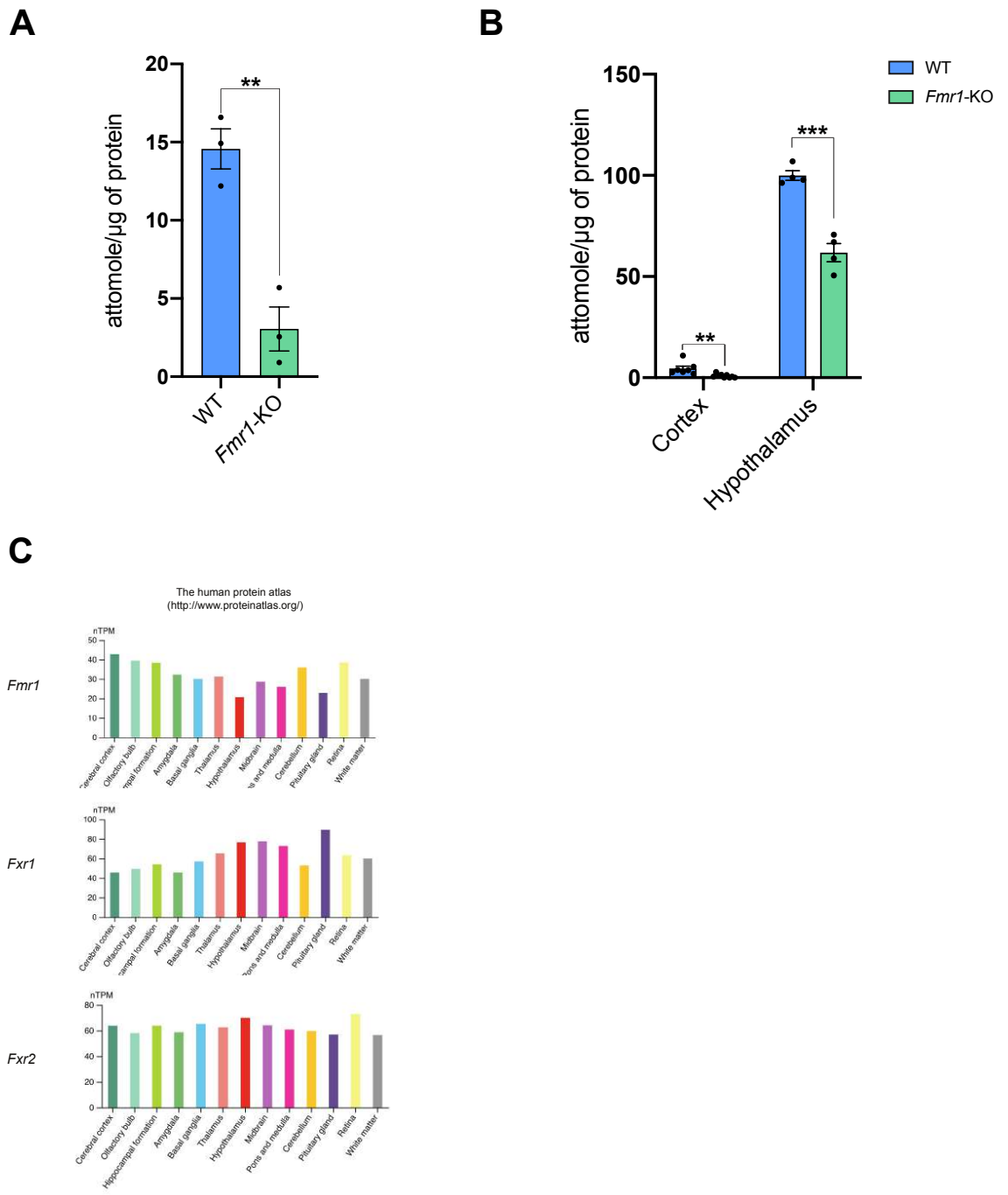

1750

1751

Supplementary Figure 4

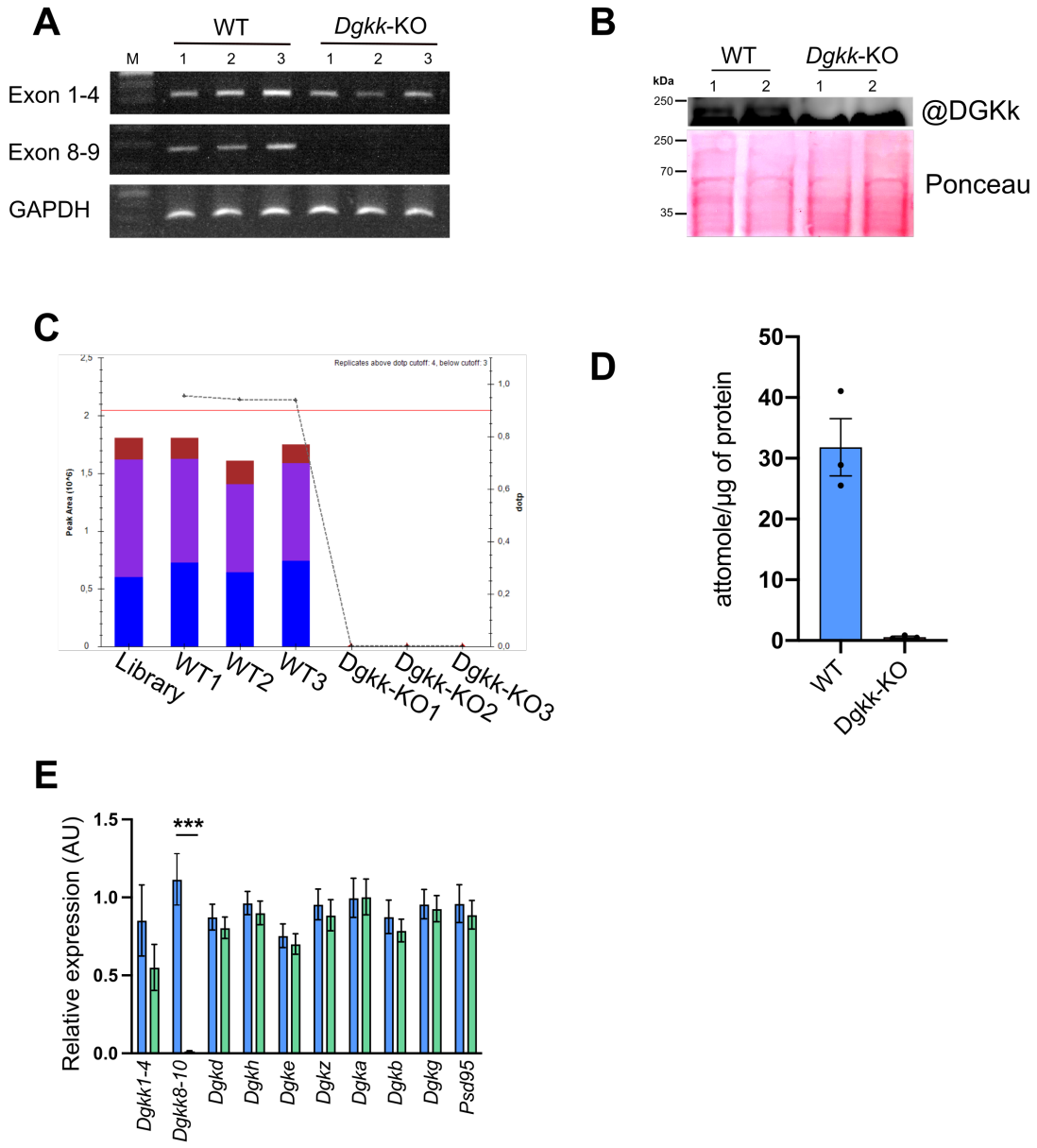

1752

Supplementary Figure 4

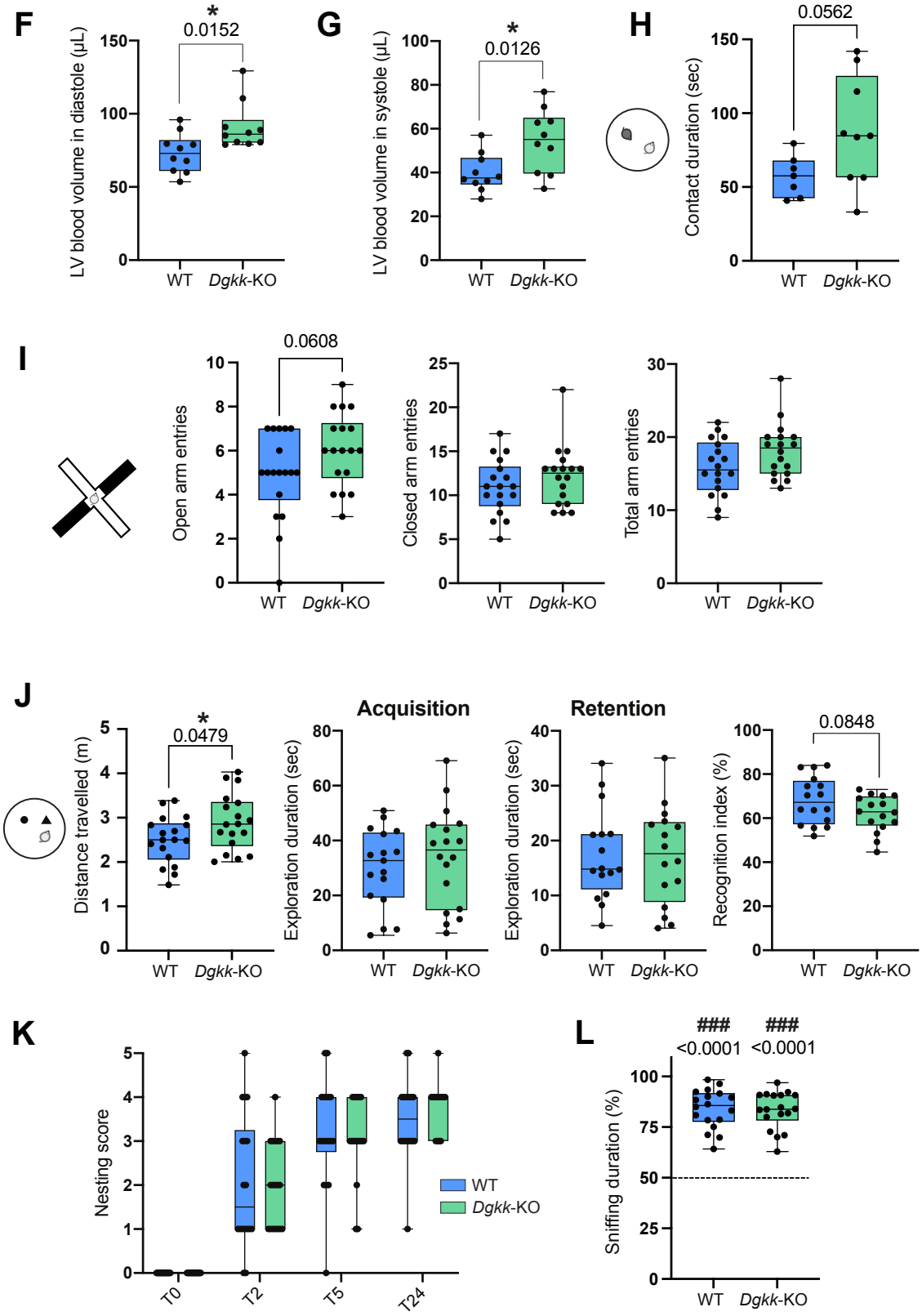

1753

Supplementary Figure 5

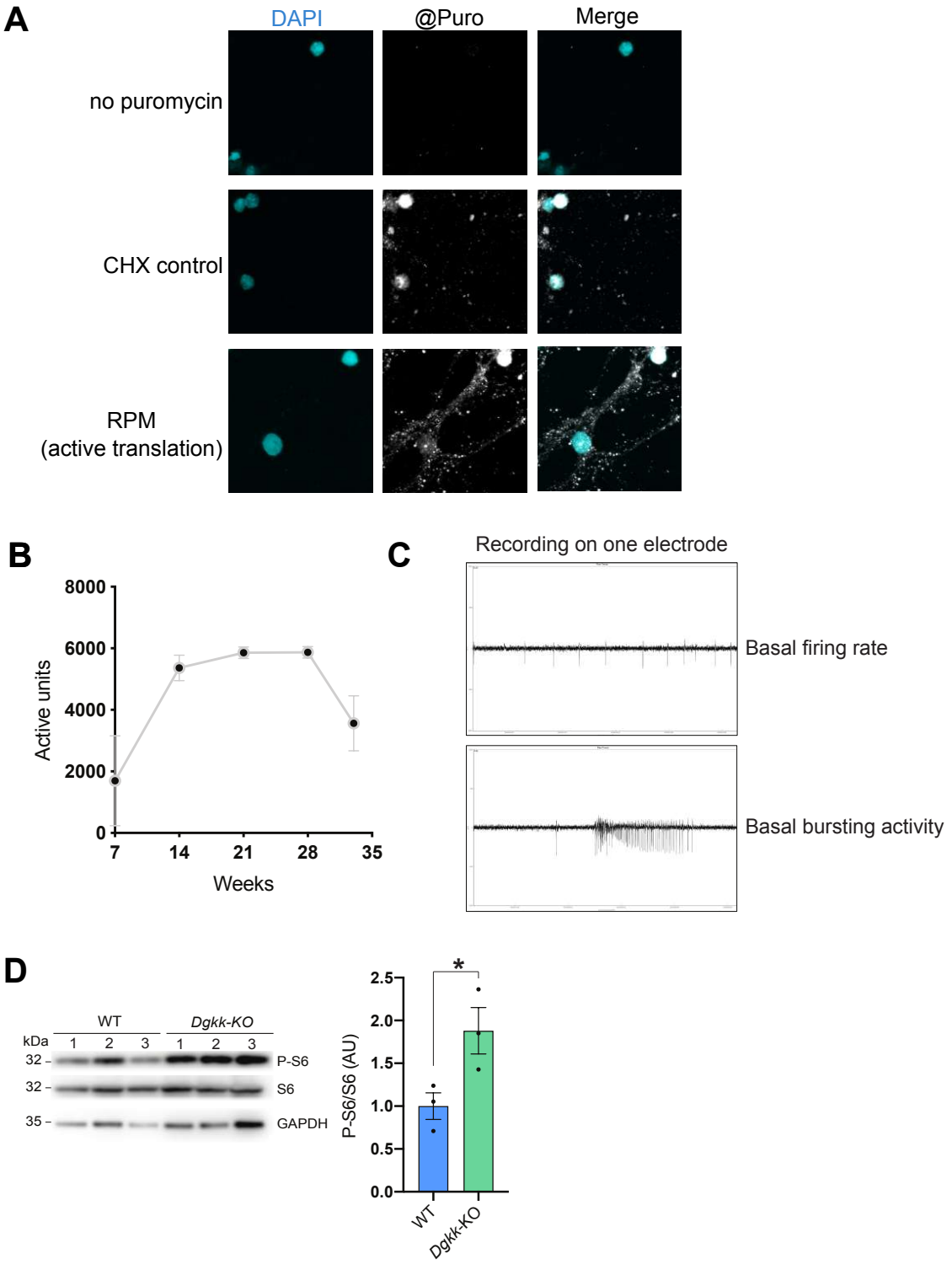

1754
1755

Supplementary Figure 6

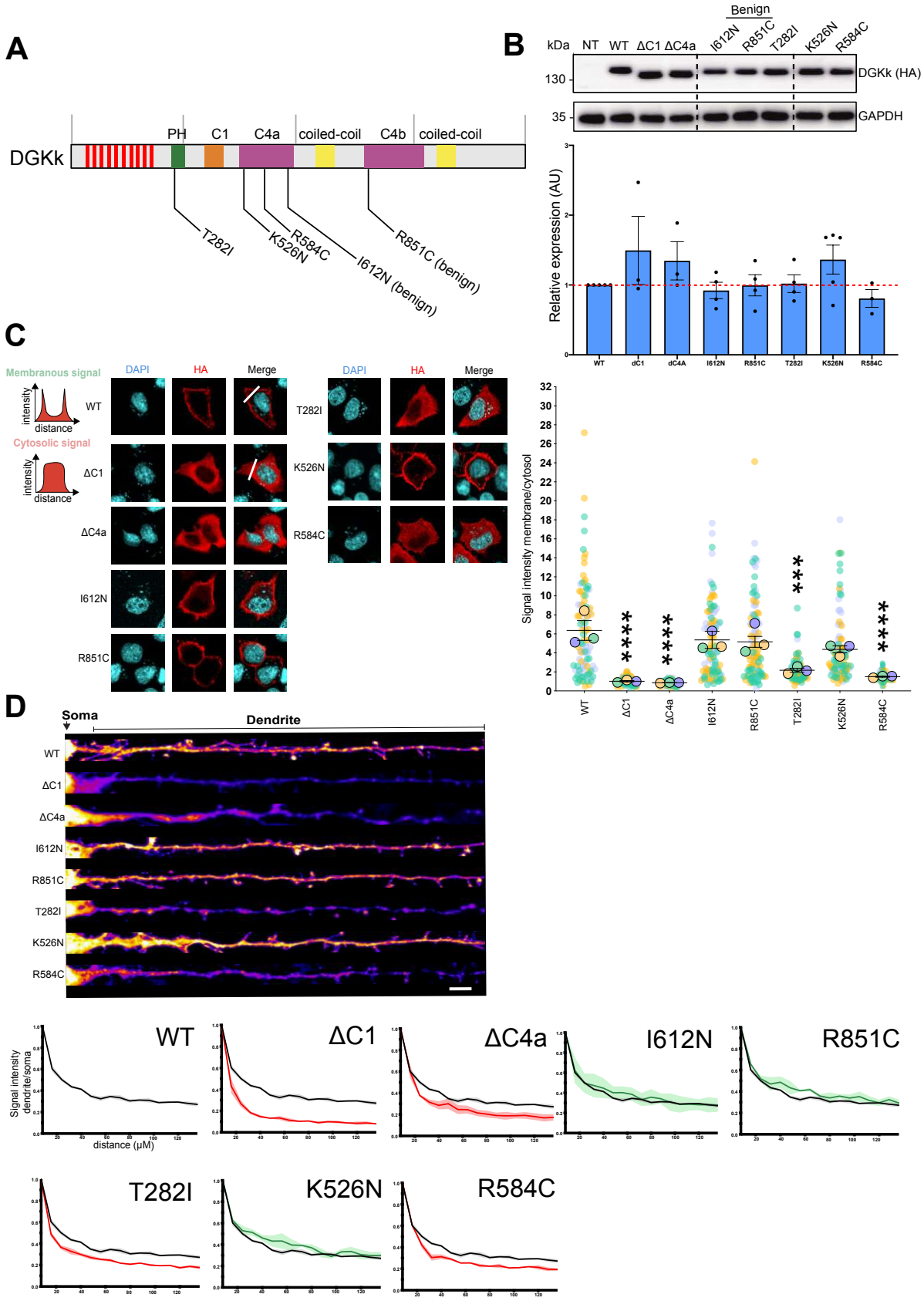

1756

Supplementary Figure 7

A

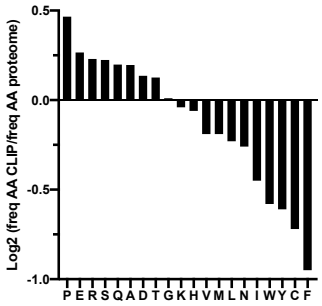

B

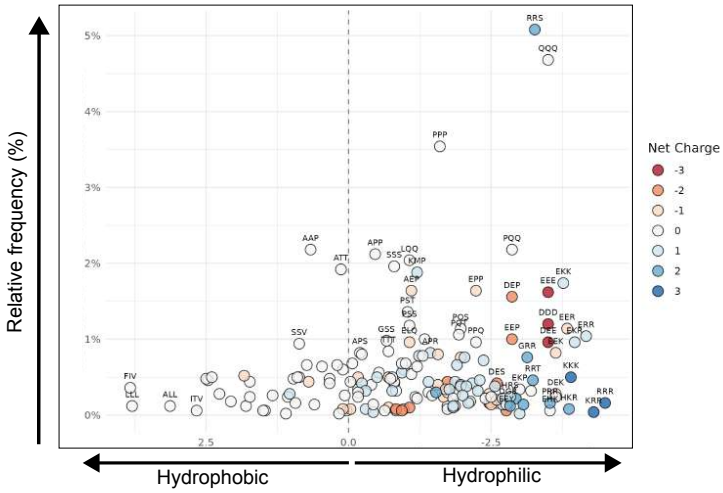

C

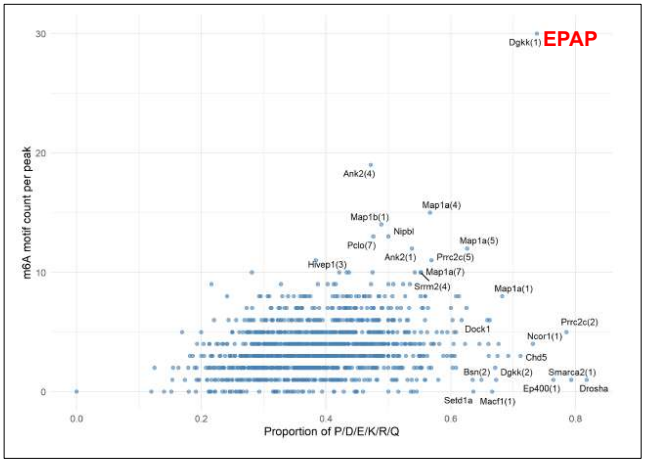

D

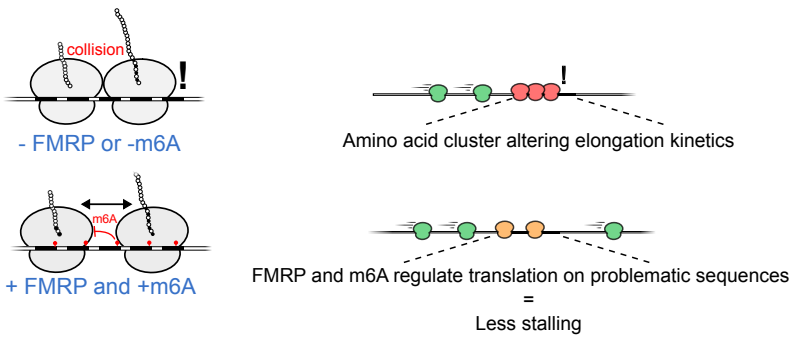

Supplementary table S1.xlsx

Supplementary table S2.xlsx